学位論文（要約）

Doctoral Dissertation (Censored)

Photo-oxidation of ferrous iron: Implications for hydrogeochemistry of early lakes on Gale Crater, Mars

（二価鉄の光酸化：火星ゲイルクレータ古湖の水文地球化学への示唆）

令和 3 年 12 月博士（理学）申請

東京大学大学院理学系研究科

地球惑星科学専攻

田畑　陽久

Abstract

Lines of geological records obtained by Mars exploration suggest that Mars once had liquid water on its surface and that the water environment experienced acidification and oxidation about 3.5 billion years ago. Since the record of liquid water on the surface disappears at 3.5 billion years ago, revealing the acidification and the oxidation mechanism is important for understanding the evolution of the Martian surface. To reconstruct the early Martian hydrogeochemistry, in this thesis, I focused on the ferrous iron (Fe(II)) photo-oxidation mechanism.

When UV light of wavelength at < 300 nm is irradiated onto an aqueous solution containing dissolved Fe(II) salts, Fe^{2+} ions are photo-oxidized to ferric iron (Fe(III)) through producing H^+ via the following equation:

$$Fe^{2+} + 3H_2O \xrightarrow{h\nu} Fe(OH)_3 + 2H^+ + 0.5H_2.$$

The reaction rate of the photochemical reaction is determined by experimentally measuring the quantum yield (i.e., the number of Fe(III) produced per the number of photons absorbed). However, previous studies have quantified the quantum yield of Fe(II) photo-oxidation only at pH < 3 due to the difficulty avoiding the oxidation by the dissolved O_2, which the reaction rate increases exponentially as pH increases. Since the pH of the early Mars aqueous environment is estimated to be pH ~7, it was not possible to apply it for the Martian aqueous environment. Furthermore, at neutral pH, a fraction of the dissolved Fe(II) ion is converted to $FeOH^+$, which could absorb photons of wavelength at < 460 nm, and the quantum yield of $FeOH^+$ photo-oxidation has not been reported.

In Chapter 2 of this thesis, I performed a laboratory experiment of Fe(II) photo-oxidation utilizing an Ar-purged glovebox and a zirconia pump deoxygenating system, which could achieve low O_2 partial pressure of < 10^{-15} bar. By preparing the pH buffer solution inside the glovebox, the quantum yields of Fe^{2+} photo-oxidation (φ_{Fe2+}) at pH of 2.0–7.6 was measured as follows:

$$\varphi_{Fe2+} = 0.103\ (\pm\ 0.005) + 2.17\ (\pm\ 0.27) \times [H^+]^{0.5}.$$

The quantum yield of $FeOH^+$ was also measured to be 0.08 ± 0.01 at pH 7.1–7.6 by adjusting the irradiation spectra of the light source to the wavelength of > 300 nm using an optical filter.

To evaluate the wavelength dependence of $FeOH^+$ photo-oxidation, experiments with the irradiation wavelength at > 200 nm, > 260 nm, and > 300 using optical filters against solutions without pH buffer were performed to investigate the timescale of acidification (Chapter 3). The quantum yields of $FeOH^+$ photo-oxidation were obtained from the initial reaction rate to be 0.13 ± 0.03 and 0.09 ± 0.01 for irradiation with a wavelength of > 260 nm and > 300 nm, respectively. The about 1.4 times higher quantum yield at irradiation of > 260 nm compared to > 300 nm suggests that although the quantum yield of $FeOH^+$ photo-oxidation shows a wavelength dependence, its variation is relatively small.

On the course of irradiation, while the solution pH drastically decreased to pH ~4 when irradiated with > 200 nm, it remained circum-neutral pH of ~6 for irradiations with > 260 nm and > 300 nm within the experimental time. Using the obtained reaction rate, the acidification timescale for Martian solar flux under various CO_2–SO_2 atmospheric compositions were calculated. It was found that although the reaction rate seems slow, $FeOH^+$ photo-oxidation would acidify the surface water pH to ~4 within a short timescale of ~10^2 years. Since various episodic warming mechanism has been proposed to sustain surface water for > 10^2 years, this result suggests the existence of a pH buffering mechanism on early Mars.

In order to constrain the geochemical conditions on Hesperian Mars, the reaction rates of Fe(II) photo-oxidation derived in Chapter 2 are applied to a reaction-transport model simulating the early Gale lake settings (Chapter 4). The appearances of oxidizing Fe oxides (e.g., hematite) in the coarser sediments and reducing Fe oxides (e.g., magnetite) in the finer sediments discovered by the Curiosity rover landed in the Gale Crater have led to a hypothesis that early Gale lakes could have been redox stratified. Fe(II) photo-oxidation could have created a vertical redox gradient because the oxidation tends to proceed near the surface due to an attenuation of solar photons. I constructed a one-dimensional geochemical model that aimed to investigate Fe(II) input fluxes, Fe(II) source (via rivers or groundwater), advection rate of the water column, pH of lake water, and atmospheric compositions to achieve redox stratification on early Gale lakes.

The results suggest that when Fe(II) is supplied via rivers, both acidic pH of 5 and a high Fe input flux are required for redox stratification. This is because dissolved Fe(II) supplied from the top layer needs to be transported to a deep part before Fe(II) photo-oxidization for redox stratification and because Fe(II) photo-oxidation rates are low at low pH. On the other hand, when Fe(II) is supplied via groundwater upwelling, redox stratification occurs in a wide range of parameters (pH 5–7) and moderate Fe input flux as long as the advection rate is kept small. High input fluxes of Fe(II) or CO_2 partial pressure of ~bar result in saturation with Fe(II)-carbonate, which is inconsistent with the in-situ observations detecting almost no carbonate minerals. Considering the recent estimate of the circum-neutral pH of early Gale lakes, these results prefer scenarios that Fe(II) was supplied via groundwater upwelling on paleo-Gale lakes. Required low advection rates imply that the depth of early Gale lakes would have been relatively deep (i.e., several hundred meters). Preferred low CO_2 in the atmosphere suggests a need for an abundance of other efficient greenhouse effect gases than CO_2 to warm the surface on early Mars.

A groundwater-supported aqueous environment on early Mars has been suggested in numerous locations based on geomorphological analyses. This thesis adds new hydrogeochemical constraints by combining laboratory experiments of Fe(II) photo-oxidation and hydrogeochemical model, utilizing the in-situ geochemical data obtained by the rover. A number of planned and ongoing planetary missions (e.g., Perseverance rover, ExoMars, MMX) are equipped with instruments capable of geochemical analyses. Therefore, the importance of understanding the fundamental geochemical processes in the planetary environments, as pursued in this thesis, is increasing.

Contents

Chapter 1. General Introduction

本章については、5 年以内に雑誌掲載等の形で公開予定のため非公開とする。

Chapter 2. An experimental study on photo-oxidation reactions of ferrous iron: Quantum yields at pH 3–7

2.1. Background of quantum yield of photo-oxidation of ferrous iron

Photo-oxidation of dissolved ferrous iron (Fe(II): Fe^{2+} and $FeOH^{+}$ at pH < 8) would have been a predominant process involved in the formation of ferric iron (Fe(III)) (hydro)oxides in aqueous environments on early Mars (e.g., Hurowitz et al., 2010, 2017). Through this reaction, the pH of surface water could have decreased to 2–4, which is consistent with the occurrence of jarosite—an Fe(III) hydrous sulfate that is thermodynamically stable at acidic pH—at Meridiani Planum (Tosca et al., 2005). Photo-oxidation of Fe(II) might also have generated Fe(III) (hydro)oxides in early lakes at Gale Crater on early Hesperian Mars (Hurowitz et al., 2017) (see Sec. 1.2).

Photo-oxidation of Fe(II) could have proceeded under a range of pH conditions in aqueous environments on early Mars. Previous studies have suggested that the pH of early Gale lakes would have been circumneutral (Bristow et al., 2017; Hurowitz et al., 2017) to weakly alkaline (Fukushi et al., 2019), based on the mineralogy of lacustrine sediments at Gale Crater. On early Mars, the pH of groundwater would have been near neutral to alkaline, owing to water-rock interactions involving mafic rocks (e.g., Zolotov and Mironenko, 2016; Kite and Melwani Daswani, 2019). At locations where upwelling of groundwater occurred, photo-oxidation would thus have proceeded in circumneutral to alkaline water (Hurowitz et al., 2017).

Although Fe(II) photo-oxidation would have proceeded under a range of pH conditions in aqueous environments on early Mars (e.g., Zolotov and Mironenko, 2016; Kite and Melwani Daswani, 2019; Fukushi et al., 2019), the quantum yield φ (defined as the number of oxidized ferrous ions divided by the number of photons absorbed by ferrous ions) were determined for a limited pH range of 0.4–3.0 previously (Jortner and Stein, 1962a, 1962b). Previous experimental studies investigated the pH dependence of the reaction at pH > 3 (Braterman et al., 1983, 1984; Konhauser et al., 2007; Nie et al., 2017). However, quantum yields at pH > 3 contained large uncertainties because photon fluxes were not measured (Braterman et al., 1983; 1984; Konhauser et al., 2007; Nie et al., 2017)

(Sec. 1.3).

Jortner and Stein (1962b) reported an empirical relationship for pH and quantum yield for Fe(II) photo-oxidation based on the experimental data obtained at pH 0.4–3.0 (see Eq. 1–2 in Part 1). As pH increases above 6, $FeOH^+$ becomes a predominant Fe(II) species in solution (Fig. 1–1a). Since Eq. 1–2 was obtained only to the pH range of 0.4–3.0, and since Fe^{2+} and $FeOH^+$ have different UV absorptivity spectra (Fig. 1–1b; Anbar and Holland, 1992; Ehrenfreund and Leibenguth, 1970), Eq. 1–2 cannot be simply extrapolated to a higher pH to calculate the photo-oxidation rate of Fe(II).

Furthermore, the experimental studies, from which Eq. 1–2 was derived, employed only a Hg lamp as a light source (Jortner and Stein, 1962b). This limits the applicability of Eq. 1–2 because the solar spectrum is continuous and markedly different from that of a Hg lamp. If there is a wavelength dependence of quantum yield, Eq. 1–2 cannot be used to determine contributions of photo-oxidation in precipitating Fe(III) (hydro)oxides on early Mars.

A major difficulty in estimating photo-oxidation quantum yields at pH > 3 is the avoidance of oxidation of aqueous Fe(II) by dissolved O_2. The rate of oxidation of aqueous Fe(II) by O_2 increases with O_2 concentration and pH (e.g., Stumm and Lee, 1961; Kanzaki and Murakami, 2013);

$$-d[Fe^{2+}]_{tot}/dt = k[Fe^{2+}]_{tot}[O_2]^x[OH^-]^2 \quad (2–1)$$

where [X] denotes the molar concentration of species X in solution; $[Fe^{2+}]_{tot} = [Fe^{2+}] + [FeOH^+]$ (at pH < 8); k is the reaction constant; and x is the reaction order with respect to O_2 (0.5–1). The rate of Fe^{2+} oxidation by O_2 can be comparable to, or even greater than, the expected photo-oxidation rates at circumneutral pH (e.g., Anbar and Holland, 1992) if O_2 concentrations reach to 1 ppm (= 3.1×10^{-5} mol L^{-1}). The 1 ppm of O_2 were, in general, involved in the previous experiments on photo-oxidation of Fe(II) (Braterman et al., 1983, 1984; Nie et al., 2017). Dissolved O_2 concentrations of << 1 ppm are thereby necessary for quantitative measurements of Fe^{2+} photo-oxidation rates at circumneutral pH.

In this study, Fe(II) photo-oxidation experiments were conducted utilizing a glovebox connected with a gas-circulating system, in which dissolved O_2 concentrations of < 0.01 ppm were achieved. This system allows us to obtain quantum yields at pH > 3. Based on the results, we discuss the pH and wavelength dependences of photo-oxidation of Fe^{2+} and $FeOH^+$.

2.2. Methods of photo-oxidation experiments to obtain quantum yields

The experimental setup of the Fe(II) photo-oxidation is illustrated in Fig. 2–1. The system was mainly composed of a reaction vessel and a light source. Experimental solutions were prepared in a glovebox and then were introduced into the quartz reaction vessel with a volume of 500 mL (diameter 8 cm, height 10 cm; Fig. 2–1). The quartz glass was chosen as it transmits more than 90% of light at a wavelength of 200–460 nm (e.g., Kitamura et al., 2007). The detailed descriptions of the procedure, light source, and reactant solutions are shown below in Secs. 2.2.1, 2.2.2, and 2.2.3, respectively. During the irradiation of UV light onto the experimental solution, a part of the solution was collected for the measurements of Fe(II) concentration. The detailed descriptions of the measurements and data analyses are shown below in Secs. 2.2.4 and 2.2.5, respectively. The reaction conditions are summarized in Sec. 2.2.6.

2.2.1. Solution preparation

Solutions containing Fe(II) ions were prepared and sealed in the reaction vessel within a 180-L Ar-purged, acrylic glovebox connected to a deoxygenation system (SiOC-2000GB; STLab Co., Japan) to provide low-O_2 conditions ($[O_2] \leq 0.01$ ppm). The detailed descriptions of the glovebox can also be found in Kanzaki and Murakami (2019) and Tabata et al. (2021).

Before preparation of solutions, the glovebox was purged for 10 hours using pure Ar gas (>99.9999 vol.%, Nissan Tanaka Corp., Japan), after which the remaining gas was circulated through the deoxygenation system for ~10 hours to remove remaining O_2. The partial pressure of O_2 (pO_2) within the glovebox was decreased to $<10^{-15}$ bar during this procedure.

When pO_2 was $< 10^{-15}$ bar in the glovebox, the pH buffer solution described below was bubbled with Ar gas at 1.4 L min^{-1} for over 4 hours for deoxygenation. Concentrations of dissolved oxygen (DO) in solutions were monitored during bubbling using a DO meter (TOX-02H; Toko Kagaku, Japan) until levels were below the detection limit ($[O_2] \leq 0.01$ ppm) (Fig. 2–2).

After deoxygenation, dissolved Fe(II) as $Fe(NH_4)_2(SO_4)_2$ powder (purity >99%; Wako Pure Chemical Industries (WPCI), Japan) was added to the buffer solution. and its pH was adjusted by adding H_2SO_4 (purity > 99%; WPCI) for pH < 3, HNO_3 (purity > 99%; WPCI) for pH 4–5, and bis-tris $C_8H_{19}NO_5$ (purity >99%; Dojindo Laboratories, Japan) for pH 6–7.6. Ultrapure Milli-Q water (18.2 MΩ; Millipore) was used as a solvent for the

buffer solutions, and pH was measured using a pH meter (LAQUAtwin pH-33; Horiba, Japan). Use of H_2SO_4 as the buffer at pH < 3 is in accord with Jortner and Stein (1962a; 1962b) and thus enables us to examine the validity of our experimental setup by comparing the results. The solution pH was stabilized using the above buffers within a range of ± 0.2 during the experiments.

2.2.1. Experimental procedure

Prior to an irradiation of the light source, the reaction vessel was filled with deoxygenated experimental solution, tightly sealed, and covered with a weighed sheet of aluminum foil inside the glovebox. Then, the reaction vessel was taken out of the glovebox and weighed to measure the initial amount of the experimental solution. The reaction vessel was set on a thermostat-magnetic stirrer at a distance of 20 cm from the lamp (Fig. 2–1). The solution was kept at room temperature (~25°C) and stirred continuously. The lamp was turned on 30 minutes before starting the irradiation to ensure that the photon flux was stabilized.

At intervals during the experiment, ~1 mL of irradiated solution was collected as a sample after another ~1 mL of solution was drained to waste through a Teflon sampling cock. This was done because the first 1 mL may contain unmixed solution from near the cock. In both the draining and sampling procedures, the solution was withdrawn from the reaction vessel by injecting 1 mL of pure He into the vessel through the butyl-rubber plug, using a gas-tight syringe (Fig. 2–1). About half (i.e., ~0.5 mL) of each collected sample was used for pH measurement, and the other half for Fe(II) concentration ($[Fe^{2+}]_{tot}$ = $[Fe^{2+}]$ + $[FeOH^+]$) measurement. Samples collected for $[Fe^{2+}]_{tot}$ measurement were introduced directly into polypropylene vessels filled with acidic solution buffered at pH 3.5 to avoid oxidation of Fe^{2+} by air after sampling. The oxidation of Fe^{2+} by atmospheric O_2 is negligible at pH < 3.5; Eq. 2–1; (Stumm and Lee, 1961; Kanzaki and Murakami, 2013). At low pH, all dissolved Fe(II) was supposed to be converted to Fe^{2+}, which can be quantified using the phenanthroline method.

The irradiation time for each experiment was set to ensure that the total fraction of oxidized Fe^{2+} ions did not exceed the initial concentration of Fe^{2+} by more than a few percent. This was done because the UV absorption by Fe(III) (hydro)oxide particles can be safely assumed to be negligible compared with absorption by aqueous Fe^{2+} ions (Sec. 2.2.5). The precipitated Fe(III) (hydro)oxide particles are known to adsorb dissolved Fe(II) species and catalyze oxidation reaction by dissolved O_2 (Tamura et al., 1976; Sung and Morgan, 1980). Although the catalyzed oxidation by the dissolved O_2 would be

negligible due to reduced [O_2] (Sec. 2.2.1) (Sung and Morgan, 1980), the high fraction of adsorbed Fe(II) could reduce the apparent photo-oxidation rate. However, the ratio of the adsorbed Fe(II) ([Fe^{2+}]$_{ad}$) to the remaining dissolved [Fe^{2+}] is reported to be linearly proportional to ([Fe^{2+}]$_{ad}$/[Fe^{2+}] = K_{ad}[Fe(III)]/[H^+], where K_{ad} is the constant = $10^{-9.6}$ mol mg^{-1}) (Tamura et al., 1976). Thus, the adsorbed fraction of Fe(II) would remain < 1% of the total Fe(II) in the solution even at pH 7, as long as [Fe(III)] is kept at below a few percent of the initial [Fe^{2+}] (i.e., 10^{-3} mol L^{-1}, see Sec. 2.2.5 below). Photo-oxidation quantum yields were calculated on the basis of the dissolved Fe(II) concentrations of the samples (Sec. 2.2.6).

2.2.3. Light sources and photon-flux actinometry

In most experiments, a 150 W Xe lamp (L7810; Hamamatsu Photonics, Japan) was used as the light source, although a low-pressure Hg lamp (80-1057-01; BHK Inc., USA) was used in some experiments to compare quantum yields with those obtained in the previous studies (Jortner and Stein, 1962a; 1962b). We used an optical filter that passes through photons with a wavelength of > 300 nm in some experiments in order to investigate the quantum yields of $FeOH^+$ photo-oxidation.

A low-pressure Hg lamp provides UV light at 254 nm wavelength (λ), and a Xe lamp provides light continuously from UV (λ > 200 nm) to visible wavelengths, with the spectrum of the latter being similar to solar spectra in the UV range (Fig. 2–3). The spectrum of the low-pressure Hg lamp in Fig. 2–3 was obtained using a calibrated UV-Vis spectrometer (USB4000; Ocean Optics, USA). An optical filter with >99% cutoff at λ = 300 nm (N-WG-320; Schott AG, Germany) was used with the Xe lamp in $FeOH^+$ experiments, allowing oxidation of Fe(II) ions to be attributed solely to photo-oxidation of $FeOH^+$ (Fig. 1–1b). The optical filter was set to the aperture of the Xe lamp (Fig. 2–1).

Since the irradiated light from the Xe lamp includes photons with the minimum energy required of photolysis of liquid H_2O (~6 eV: corresponding to a photon with a wavelength of ~200 nm) (Sander et al., 1993; Bernas et al., 1997), reactive oxygen species could be generated via H_2O photolysis in our experiments. However, UV absorptivity of liquid H_2O at 200 nm is 0.0026 cm^{-1} (Fewell and Trojan, 2019), which is an order of magnitude lower than that of Fe^{2+} at the concentration of 10^{-3} mol L^{-1} in our experiments (0.0286 cm^{-1}) (Heinrich and Seward, 1990). Also, the quantum yield of H_2O photolysis is reported to be in the order of 0.001 by a photon at ~180 nm (Nikogosyan et al., 1983), which is two orders of magnitude lower than that of Fe^{2+} photo-oxidation (see Sec. 2.3 and the previous studies (e.g., Jortner and Stein, 1962a)). Thus, the contribution of oxidants

produced via H_2O photolysis to oxidize Fe^{2+} is more than three orders of magnitude smaller than Fe^{2+} photo-oxidation. Furthermore, the effect of H_2O photolysis should be even smaller because Fe^{2+} can utilize photons of 200–300 nm for photo-oxidation, unlike H_2O.

Photon fluxes of wavelengths at 200–460 nm were quantified using the potassium ferrioxalate ($K_3[Fe^{(III)}(C_2O_4)_3]$) actinometry method (e.g., Hatchard and Parker, 1956; Kuhn et al., 2004), in which dissolved Fe(III) of potassium ferrioxalate is photo-reduced to Fe(II) when potassium ferrioxalate solution is irradiated at $\lambda < 460$ nm (Eq. 2–2).

$$[Fe^{(III)}(C_2O_4)_3]^{3-} \xrightarrow{h\nu} [Fe^{(II)}(C_2O_4)_3]^{2-} + C_2O_4^{-} \quad (2\text{–}2)$$

With a known photo-reduction quantum yield (Fig. 2–4), the photon flux can be determined through measurement of photo-reduced $[Fe^{2+}]$ (see Sec. 2.2.4) in the potassium ferrioxalate solution upon irradiation (Eq. 2–3):

$$I_{abs,f} = \frac{[Fe^{2+}]}{\varphi_f t} \quad (2\text{–}3)$$

where $I_{abs,f}$ is the photon flux absorbed by the ferrioxalate (mol L^{-1} min^{-1}), φ_f is the quantum yield of the photo-reduction reaction of ferrioxalate, and t (min) is the irradiation time. The geometric configuration during photon-flux measurements was the same as that of the photo-oxidation experiments.

In the photon-flux measurements, potassium ferrioxalate solution at concentrations of 6×10^{-3} or 15×10^{-3} mol L^{-1} was introduced into the reaction vessel (Table 2–1). The concentrations of ferrioxalate were chosen to ensure that the photo-reduced fraction of ferrioxalate is < 10%. The ferrioxalate was synthesized from potassium oxalate monohydrate ($(COOK)_2 \cdot H_2O$; purity > 99%; WPCI) and ferric chloride hexahydrate ($FeCl_3 \cdot 6H_2O$; purity > 99%; WPCI), following previously published methods (e.g., Kuhn et al., 2004). All procedures were conducted under a > 500-nm Safelight (PTP760; Paterson Photographic Ltd., UK) to avoid photochemical artifacts.

The Fe^{2+} concentration in potassium ferrioxalate solution increased linearly with irradiation time (Fig. 2–5). Photon flux was calculated from the quantum yield of potassium ferrioxalate (Eq. 2–3) (Murov, 1993; Goldstein and Rabani, 2008). The measured photon fluxes are summarized in Table 2–1.

2.2.4. Fe(II) concentration measurement

The total Fe(II) concentrations of samples were determined using the phenanthroline

method (e.g., Saywell and Cunningham, 1937; Kuhn et al., 2004), in which o-phenanthroline displays an absorption centered at λ = 510 nm in an acidic (pH 3.5) solution through the formation of a chelate complex with Fe^{2+}.

Phenanthroline solutions were prepared as described in Hatchard and Parker (1956). For each Fe^{2+} analysis, 2.5 mL of solution was prepared in a polypropylene tube from 1 mL 5.5 mmol L^{-1} o-phenanthroline solution (purity >99%; WPCI), 0.25 mL ultrapure water, and 1.25 mL of a mixture of 0.18 mol L^{-1} H_2SO_4 and 0.6 mol L^{-1} CH_3COONa (purity >99%: WPCI) solutions (i.e., an H_2SO_4–CH_3COONa pH buffer at pH 3.5). Each collected sample was added to a tube of a prepared solution and kept in the dark for 30 minutes to stabilize the Fe^{2+}–phenanthroline chelate complex (Kuhn et al., 2004). All these procedures were conducted under a Safelight (as above) to avoid photo-oxidation of Fe^{2+} after the sampling. Sample absorbances were measured by UV–visible spectrophotometry (Lambda 650; Perkin Elmer, USA). A calibration plot was generated with solutions of known Fe^{2+} concentration (Fig. 2–6).

2.2.5. Reaction conditions and evaluation of air contamination

Reaction conditions involved systematically varied irradiation conditions and solution pH in experiments, referred to by 'run' numbers in Table 2–2: (a) using the Hg lamp (runs 1–3); (b) using the Xe lamp without an optical filter (runs 4–9); (c) using the Xe lamp with an optical filter (runs 10–12); and (d) a control experiment using no light source (run 13). These groups of experiments were respectively intended for (a) comparison with previous studies (Jortner and Stein, 1962a; 1962b) without deoxygenation of solutions (runs 1–3); (b) study of the pH dependence of the Fe^{2+} photo-oxidation rate (runs 4–9); (c) study of $FeOH^+$ photo-oxidation (runs 10–12); and (d) a background check on the effect of Fe(II) oxidation due to O_2 contamination during the procedures (run 13). In the background check, the measured $[Fe^{2+}]$ remained unchanged from the initial value within a 1σ of measurement error ($\pm$ 6.6 × 10^{-3} mmol L^{-1}) for 600 min (Fig. 2–7), which indicates that oxidation of Fe^{2+} due to air contamination during sampling was negligible.

2.2.6. Photo-oxidation analysis

After irradiation, $\Delta[Fe^{2+}]$ was determined; i.e., the difference in $[Fe^{2+}]$ from the initial value ($[Fe^{2+}]_0$) after a certain time, t (min), of irradiation ($[Fe^{2+}]_t$): $\Delta[Fe^{2+}] = [Fe^{2+}]_0 - [Fe^{2+}]_t$. The increasing rate of $\Delta[Fe^{2+}]$ gradually decreased over the irradiation time, because Fe^{2+} is consumed by photo-oxidation, and because UV light is absorbed by

produced Fe(III) ions (Fe^{3+}, $Fe(OH)^{2+}$, and $Fe(OH)_2^{+}$). The latter reduces the photon flux absorbed by Fe(II) (i.e., absorbed photon flux, $I_{abs,Fe2+}$ and $I_{abs,FeOH+}$; unit mol min^{-1} L^{-1}), the so-called inner-filter effect (Jortner and Stein, 1962a, 1962b). In determining quantum yields of Fe^{2+} and $FeOH^{+}$ photo-oxidation (φ_{Fe2+} and φ_{FeOH+}, respectively) from $\Delta[Fe^{2+}]$, the effect of the inner-filter effects must be taken quantitatively into account as follows.

The theoretical time trend (i.e., the trend with irradiation time) of $\Delta[Fe^{2+}]$ was first considered for a given set of quantum yields, based on quantum yields, φ_{Fe2+} and φ_{FeOH+}, and absorbed photon flux, $I_{abs,Fe2+}$ and $I_{abs,FeOH+}$:

$$\Delta[\mathrm{Fe}^{2+}] = \int_0^t \varphi_{\mathrm{Fe2+}} I_{\mathrm{abs,Fe2+}}(t) + \varphi_{\mathrm{FeOH+}} I_{\mathrm{abs,FeOH+}}(t)\, dt. \qquad (2\text{–}4)$$

The functions $I_{abs,\,Fe2+}$ and $I_{abs,FeOH+}$ are represented as:

$$I_{\mathrm{abs,Fe2+}}(t) = \int_{200}^{300} I_0(\lambda)\left(1 - 10^{-k(\lambda)}\right)\frac{\varepsilon_{\mathrm{Fe2+}}[\mathrm{Fe}^{2+}]_t}{\sum \varepsilon_{\mathrm{x}}[\mathrm{X}]_t}\, d\lambda \qquad (2\text{–}5)$$

$$I_{\mathrm{abs,FeOH+}}(t) = \int_{200}^{460} I_0(\lambda)\left(1 - 10^{-k(\lambda)}\right)\frac{\varepsilon_{\mathrm{FeOH+}}[\mathrm{FeOH}^{+}]_t}{\sum \varepsilon_{\mathrm{x}}[\mathrm{X}]_t}\, d\lambda \qquad (2\text{–}6)$$

where $I_0(\lambda)$ is the irradiated photon flux at wavelength λ (mol cm^{-2} min^{-1} nm^{-1}), ε_X is the molar absorptivity of species X (mol^{-1} L cm^{-1}), and $k(\lambda)$ represents the total absorption due to all dissolved species. The function $k(\lambda)$ is expressed as:

$$k(\lambda) = \sum \varepsilon_{\mathrm{X}}[\mathrm{X}]d \qquad (2\text{–}7)$$

where d is the optical path length (6.3 cm was used as an average optical path length based on the geometry of the reaction vessel). To obtain $k(\lambda)$, the respective concentrations of Fe^{2+}, $Fe(OH)^{+}$, Fe^{3+}, $Fe(OH)^{2+}$, and $Fe(OH)_2^{+}$, based on ion speciation in a solution at 25ºC for the pH of the experiment, were applied (Fig. 2–8) (Stefansson, 2007). Assuming that Fe(III) ions formed solely during photo-oxidation of Fe^{2+}, the total concentration of Fe(III) ions ($[Fe^{3+}]_{tot} = [Fe^{3+}] + [Fe(OH)^{2+}] + [Fe(OH)_2^{+}]$) was treated as per $\Delta[Fe^{2+}]$ as long as its value was lower than the solubility of ferrihydrite ($Fe(OH)_3$; an initial Fe(III) precipitation phase; Stefansson (2007)). When $\Delta[Fe^{2+}]$ exceeded the solubility of ferrihydrite, the concentrations of Fe(III) ions were assumed to be in equilibrium with the solubility of ferrihydrite at the applied pH. Published values were used for the molar absorptivity (ε_X) of each species (Heinrich and Seward, 1990; Anbar and Holland, 1992; Stefansson, 2007; Fig. 1–1 and Fig. 2–8). For Fe(III) ions, ε_X was assumed to be zero at λ > 350 nm for Fe^{3+}, >400 nm for $FeOH^{2+}$, and >400 nm for

$Fe(OH)_2^+$, because ε_X decreases markedly at longer wavelengths (and no published values for longer wavelengths were available). Measured total Fe(II) concentrations and published ε_X values were used to calculate $k(\lambda)$ for the applied pH. The spectral irradiated photon flux, $I_0(\lambda)$, was calculated by scaling the manufacturer-specified spectral irradiance (Fig. 2–3) so that the integrated irradiation flux matched the photon flux measured by chemical actinometry (Table 2–1). For the Hg lamp, the measured photon flux was assumed to be attributed to the emission line at λ = 254 nm (Fig. 2–3). Photon absorption calculations (Eqs. 2–5 and 2–6) involved integration over the range of λ = 200–460 nm at 10-nm intervals. The time trends of $I_{abs,\,Fe2+}$, $I_{abs,FeOH+}$, and $\Delta[Fe^{2+}]$ were then determined for a given set of quantum yields.

Quantum yields were based on least-squares fitting of experimental time trends of $\Delta[Fe^{2+}]$ with the theoretical predictions of $\Delta[Fe^{2+}]$. The $FeOH^+$ concentration becomes non-negligible at pH > 5 (e.g., runs 8 and 9; Fig. 1–1a), so the time trend of $\Delta[Fe^{2+}]$ at pH > 5 could be caused by photo-oxidation of both Fe^{2+} and $FeOH^+$. To distinguish between these reactions, φ_{FeOH+} was first obtained using the optical filter (runs 10–12), then employed in the photo-oxidation analyses to obtain φ_{Fe2+} based on the time trend of $\Delta[Fe^{2+}]$ at pH > 5. Errors in quantum yields were evaluated by the propagation of uncertainties and errors in measurements and calculations, applying 1σ uncertainties for $\Delta[Fe^{2+}]$, $[Fe^{2+}]_0$, and I_0. The calculated errors in quantum yields were ≤ 10%.

In the analysis, reductive dissolution of Fe(III) (hydro)oxides by dissolved H_2 was not considered. Although the kinetic rate of such a reaction is not reported, a decrease in photo-oxidation rate would be observed if such a reaction occurs. However, as shown in Sec. 2.3, the time evolutions of photo-oxidation rates are quantitatively explained by the inner-filter effect, suggesting the reductive dissolution of Fe(III) (hydro)oxides by H_2 is less important, possibly due to the low solubility of H_2 in water. The precipitation of Fe(II) (hydro)oxide, $Fe(OH)_2$, was also not considered as its precipitation is negligible at the experimental pH of this study (Fig. 1–1a).

2.3. Results

2.3.1. Fe^{2+} photo-oxidation at 254 nm

Time trends of $\Delta[Fe^{2+}]$ during UV irradiation with the Hg lamp with $[Fe^{2+}]_0$ = 0.02, 0.01, and 0.001 mol L^{-1} (runs 1–3, respectively) are shown in Fig. 2–9, where an increase in $\Delta[Fe^{2+}]$ indicates consumption of Fe(II) species. Throughout the experiments, the measured $\Delta[Fe^{2+}]$ values increase continuously with Fe^{2+} photo-oxidation (Fig. 2–9).

However, the rate of increase decreases gradually, owing to the inner-filter effect (see Sec. 2.2.6). By fitting the measured time trend of $\Delta[Fe^{2+}]$ with the theoretical equation by Eqs. 2–4 to 2–6 for $\Delta[Fe^{2+}]$, the quantum yields of Fe^{2+} photo-oxidation, φ_{Fe2+}, for runs 1–3 were determined as 0.29 ± 0.03 (at pH 0.5), 0.29 ± 0.03 (at pH 0.6), and 0.24 ± 0.02 (at pH 0.4), respectively (Fig. 2–10), which are consistent with yields reported previously using a similar Hg lamp (Jortner and Stein, 1962a; Fig. 2–9a), and which confirm the validity of our experimental system and procedure.

2.3.2. Fe^{2+} photo-oxidation by UV–visible light (> 200 nm)

Time trends of $\Delta[Fe^{2+}]$ during experiments with the Xe lamp (runs 4–12) are shown in Fig. 2–11. Measured $\Delta[Fe^{2+}]$ values increase with irradiation time, as well as runs 1–3 with the Hg lamp. The inner-filter effect becoming less significant as pH increases, thus increasing almost linearly against irradiation time at pH 6 compared to pH 1.9 (e.g., compare Fig. 2–11a and f). This is because the solubility of ferrihydrite decreases exponentially as pH increases from 2 to 7 (Stefansson, 2007). The fraction of photons absorbed by aqueous Fe(III) ions (Fe^{3+}, $Fe(OH)^{2+}$, and $Fe(OH)_2^{+}$) decreases markedly at higher pH, resulting in an almost linear increase in $\Delta[Fe^{2+}]$ with irradiation time (Fig. 2–11).

Measured quantum yields of Fe^{2+} photo-oxidation, φ_{Fe2+} are plotted against pH in Fig. 2–12. Their decrease as pH increases can be fitted by the function:

$$\varphi_{Fe2+} = 0.103\ (\pm 0.005) + 2.17\ (\pm 0.27) \times [H^+]^{0.5}. \quad (2\text{–}8)$$

Here, the contribution of $FeOH^+$ photo-oxidation is excluded using the quantum yield obtained in runs 10–12 (see the next section; also Sec. 2.2.6). Thus, φ_{Fe2+} represents the quantum yield solely by photo-oxidation of Fe^{2+}. Jortner and Stein (1962a, 1962b) reported a similar pH dependence (the $\propto [H^+]^{0.5}$ term) for quantum yield at pH 0.4–3.0 with a Hg lamp (Eq. 1–2) and attributed it to a reaction mechanism where electrons (i.e., H atoms) produced by photo-oxidation of Fe^{2+} are consumed more effectively in solutions with higher H^+ concentrations.

The effective quantum yield of Fe^{2+} photo-oxidation is determined by the sum of the three following processes: 1. Photo-oxidation of UV-excited Fe^{2+} ($Fe^{2+}(OH)_2^*$) followed by an escape of hydrogen atom into the bulk solvent (Eq. 2–9), 2. Backreaction of photo-oxidation (Eq. 2–10), and 3. Backreaction inhibited by H^+ scavenging the hydrogen atom, releasing H_2^+ into the bulk solvent (Eq. 2–11).

$$Fe^{2+}(OH)_2^* + H_2O \rightarrow Fe^{3+}(OH)_3 + H_{bulk} \quad (2\text{–}9)$$

$$Fe^{3+}(OH)_3 + H \rightarrow Fe^{2+}(OH)_2 + H_2O \quad (2\text{–}10)$$

$$H^+ + H \rightarrow H_2{}^+{}_{bulk} \quad (2\text{–}11)$$

While the quantum yield via the first process (Eq. 2–9) is pH-independent, corresponding to the first term in Eq. 2–8, the quantum yield via the second and third process would be pH-dependent as the H^+ involves as a reactant. The pH dependence of such a system would be determined by the competition of the reaction of Eq. 2–10 and 2–11, which was investigated by Noyes (1955).

When the probability that the backreaction occur at a time interval between t and $t + dt$ is expressed as $h(t)$, the probability of the back reaction occurring after the photo-oxidation, β, could be written as follows:

$$\int_0^\infty h(t)\, dt = \beta. \quad (2\text{–}12)$$

Since the backreaction requires the recombination of Fe^{3+} and H, its probability would be expected to be proportional to $\propto t^{-3/2}$, assuming the 3-D random walk for Fe^{3+} and H (Noyes, 1955). Thus $h(t) = a/t^{3/2}$, where a is a constant parameter. On the other hand, the probability that H reacts with H^+ during the random walk of t min could be expressed as follows:

$$1 - e^{-2k_{11}[H^+]t,} \quad (2\text{–}13)$$

where k_{11} is the reaction rate constant of Eq. 2–11 (Noyes, 1955). Thus, the fraction that escapes the back reaction could be given by the time integration of the product of $h(t)$ and Eq. 2–13 as follows:

$$\int_0^\infty h(t)\left(1 - e^{-2k_{11}[H^+]t}\right)dt = 2a\sqrt{2\pi k_{11}[H^+]} + \cdots. \quad (2\text{–}14)$$

Here, the definite integration was conducted using the characteristics of the Gauss error function. Therefore, the result that the quantum yield shows a pH-dependence of $[H^+]^{0.5}$ suggests that the H^+ is interacting with the H atoms (i.e., electrons) produced in the photo-oxidation reaction via the scavenging processes rather than through other mechanisms.

The similar pH dependence observed here at higher pH under continuous UV–visible irradiation (Fig. 2–12) suggests a similar reaction mechanism, despite variations in solution composition and irradiation wavelength. Furthermore, if the electron consumption by H^+ fully accounts for the pH dependence of Eq. 8, then the elementary process of the Fe^{2+} photo-oxidation itself could be pH-independent.

Although our measured quantum yields display a similar pH dependence to those obtained under the Hg lamp, the absolute values using the Xe lamp are significantly

different from previous ones using the Hg lamp (Fig. 2–12). For example, the yield at pH 1.9 (run 4; φ_{Fe2+} = 0.34 ± 0.03) obtained using the Xe lamp in deoxygenated solution is higher than that reported previously using the Hg lamp against deoxygenated solutions (φ_{Fe2+} ~0.1 at pH 1.9; Jortner and Stein, 1962b; Fig. 2–10). This suggests a wavelength dependence of the quantum yield of Fe^{2+} photo-oxidation, as discussed in Sec. 2.4.1.

2.3.3. $FeOH^+$ photo-oxidation

Time trends of $\Delta[Fe^{2+}]$ with the Xe lamp plus optical filter (i.e., λ > 300 nm; runs 10–12) are shown in Fig. 2–11; as explained in Sec. 2.2.3, only $FeOH^+$ can be photo-oxidized under these conditions (Fig. 1b). The low inner-filter effect (due to the low solubility of ferrihydrite at pH > 7.1) means that $\Delta[Fe^{2+}]$ values increase linearly with irradiation time (Fig. 2–11). Quantum yields of $FeOH^+$ photo-oxidation, φ_{FeOH+}, at pH 7.1, 7.4, and 7.6 were 0.071 ± 0.006, 0.096 ± 0.009, and 0.072 ± 0.006, respectively (Fig. 2–12). The investigated pH range was narrow for φ_{FeOH+} compared with that of φ_{Fe2+} because $[FeOH^+]$ is very low at pH < 7 (Fig. 1–1a), and because oxidation by dissolved O_2 cannot be excluded at pH > 8. Within the pH range of 7.1–7.6, no obvious pH dependence of φ_{FeOH+} was observed (Fig. 2–12). The measured φ_{FeOH+} value of 0.08 ± 0.01 at pH 7.1–7.6 is comparable with φ_{Fe2+} at pH ~7 (Fig. 2–12).

2.4. Discussion

2.4.1. Wavelength dependence of Fe^{2+} photo-oxidation

Our results indicate that the quantum yield of Fe^{2+} photo-oxidation by the Xe lamp (λ > 200 nm; Fig. 2–12) is significantly higher than that obtained using the Hg lamp (λ = 254 nm; Fig. 2–10), with the former representing an average over the UV–visible (λ > 200 nm) range, and the latter the yield at λ = 254 nm.

A shorter wavelength means higher energy, so the Xe lamp could produce higher φ_{Fe2+} values. Logan (1990) demonstrated that the quantum yield of Fe^{2+} photo-oxidation with UV at λ = 229 nm from a Cd lamp was 1.4 times that at 254 nm (Hg lamp). For the Xe-lamp quantum yield (φ_{Fe2+} ~0.35 at pH 2; Fig. 2–12) to be a few times that of λ = 254 nm (Hg-lamp φ_{Fe2+} ~0.1 at pH 1.9; Fig. 2–10), the yields at λ < 230 nm must be > 0.35.

In experiments with the Xe lamp, 40–50% of the total photons absorbed by Fe^{2+} ions are at λ < 230 nm, based on the integration of emission intensities from the Xe lamp (Fig. 2–3) using Eq. 2–5 to 2–7. Although the irradiation flux at λ < 230 nm is relatively small,

high absorption cross-sections of Fe(II) at $\lambda < 230$ nm (Fig. 1–1) results in such efficient absorption of photons at short wavelengths. Assuming φ_{Fe2+} values of 0.1–0.14 at $\lambda > 230$ nm at pH 2 (Jortner and Stein, 1962b; Logan, 1990), φ_{Fe2+} at λ = 200–230 nm must be 0.5–0.6 to account for the average φ_{Fe2+} of 0.35 obtained in our experiment with irradiation at $\lambda > 200$ nm (Fig. 2–3).

The quantum yield of 0.5–0.6 may seem high compared to the previous reports (Jortner and Stein, 1962b; Logan, 1990). However, Horvath and Papp (1984) report the quantum yields of 0.6–1.0 at solution pH of –0.5–2.0 for the Cu^+ photo-oxidation reaction, which also demonstrates pH dependence of $\propto [H^+]^{0.5}$ (see Sec. 2.3.1). In the photo-oxidation reactions that the produced radicals (i.e., H atoms) are also involved in the oxidation reactions, quantum yields of the net oxidation reaction tends to be high. In fact, an apparent quantum yield of > 1.0 is observed in the experiment at a pH of –0.3, which abundant $[H^+]$ sufficiently scavenges the H atoms (Horvath and Papp, 1984).

Further systematic investigation of the wavelength dependence of the quantum yield of Fe^{2+} photo-oxidation is required, but our results indicate that Fe^{2+} photo-oxidation proceeds efficiently under irradiation at λ = 200–230 nm. UV light at λ = 200–250 nm might have reached the surfaces of early Mars when shielding by O_2 and/or O_3 was absent in their atmospheres (e.g., Ranjan and Sasselov, 2016).

2.4.2. Quantum yield of $FeOH^+$ photo-oxidation

Previous studies of $FeOH^+$ photo-oxidation used an optical filter ($\lambda > 366$ nm) with a medium-pressure Hg lamp (Braterman et al., 1983; 1984) or a borosilicate glass reaction vessel that transmits UV only at $\lambda >$ ~300 nm (Nie et al., 2017). Quantum yields of $FeOH^+$ photo-oxidation have been determined as ~0.01–0.05 (Braterman et al., 1983; 1984) or ~0.07 (Nie et al., 2017), based on concentrations of Fe^{3+} (Braterman et al., 1983; 1984) or Fe^{2+} (Nie et al., 2017) ions measured during irradiation. However, these studies involved no quantitative photon flux measurements (Nie et al., 2017), or photo-oxidation experiments without pH buffers (Braterman et al., 1983; 1984). As the concentration of $FeOH^+$ is strongly dependent on pH (Fig. 1–1a), the use of a pH buffer is crucial when determining quantum yield.

In contrast, through measurement of photon flux and usage of pH buffers, the present study determined a quantum yield, φ_{FeOH+}, of 0.08 ± 0.01 for $FeOH^+$ photo-oxidation at pH 7.1–7.6, which is consistent with that estimated at pH 7.3 (~0.07) by Nie et al. (2017). Braterman et al. (1983; 1984) might have underestimated φ_{FeOH+} (0.01–0.05) at circumneutral pH, possibly because they used no pH buffers. In that case, a decrease in

pH due to photo-oxidation could have inhibited further photo-oxidation of $FeOH^+$ (Fig. 1–1)

At pH 7.0 with no optical filter (run 9), only ~1% of the total Fe(II) ions were consumed through $FeOH^+$ photo-oxidation, with ~99% occurring through Fe^{2+} photo-oxidation. Despite the low abundance of $FeOH^+$ at pH ~7 ($[FeOH^+]/[Fe^{2+}] \approx 10^{-2.5}$) (Fig. 1–1a), the loss of Fe(II) through $FeOH^+$ photo-oxidation occurred because $FeOH^+$ mainly absorbs UV–visible light at $\lambda > 300$ nm (Fig. 1–1b). The high emission intensity of the Xe lamp at $\lambda > 300$ nm (Fig. 2–3) and the effective absorption of long-wavelength light by $FeOH^+$ result in efficient $FeOH^+$ photo-oxidation at pH ~7. In an alkaline solution (pH > 8), where $FeOH^+$ is the predominant form of Fe(II), it would enhance the overall photo-oxidation.

2.4.3. Implications for Fe photo-oxidation on early Mars

As described in Sec. 2.1, photo-oxidation of ferrous ions is suggested to be a possible mechanism to explain the depositions of Fe(III) (hydro)oxides in the middle Hesperian on Mars (e.g., Hurowitz et al., 2010; Nie et al., 2017). Nie et al. (2017) estimated the efficiency of Fe^{2+} photo-oxidation on early Mars by taking into account the wavelength dependence of the absorption. They assumed a constant quantum yield, φ_{Fe2+}, of 0.07 for Fe^{2+} photo-oxidation throughout pH 2–7 and considered no photo-oxidation of $FeOH^+$. In addition, they assumed no absorption of UV light due to Fe^{3+} ions in solutions.

As shown in Eq. 2–8, the obtained φ_{Fe2+} in our experiments is significantly higher than 0.07 that were assumed by Nie et al. (2017). In addition, we showed $\varphi_{FeOH+} = 0.08$ for $FeOH^+$ photo-oxidation (see Sec. 2.4.2), which was ignored previously (Nie et al., 2017). Accordingly, we suggest that the previous study would underestimate the efficiency of Fe^{2+} photo-oxidation on early Mars, especially in surface water with circumneutral pH. We also confirmed the occurrence of the inner-filter effects in our experiments, especially low pH. This was because at low pH, Fe^{3+} ions can be present in the solutions. Thus, we also suggest that the previous study would overestimate the efficiency of Fe^{2+} photo-oxidation in the low pH range.

In Part 4 of this thesis, we calculate the photo-oxidation rate and Fe(III) (hydro)oxide precipitation for various pH of surface water on early Mars using a one-dimensional geochemical model by introducing Eq. 2–8. Based on the model results, we will evaluate the geochemical conditions that can account for the Fe(III) (hydro)oxide precipitation on early Gale Lake (see Part 4 for the detailed results and discussion).

2.5. Summary

In the present study, the reaction rate (i.e., quantum yields; φ) of the photo-oxidation reaction of Fe(II) (Fe^{2+} and $FeOH^{+}$) were determined by conducting laboratory experiments. The semi-empirical equation of quantum yields of Fe^{2+} photo-oxidation at pH 3.0–7.6 under continuous UV–visible irradiation with wavelengths at > 200 nm using Xe-lamp was determined as follows:

$$\varphi_{Fe2+} = 0.103\ (\pm\ 0.005) + 2.17\ (\pm\ 0.27) \times [H^{+}]^{0.5}.$$

The quantum yield of $FeOH^{+}$ photo-oxidation reaction was also determined at pH 7.1–7.6, under continuous UV–visible irradiation with wavelength at > 300 nm using a UV cutoff filter, as 0.08 ± 0.01. The obtained quantum yield values were a few times higher than that reported by the previous studies at pH < 3.0 under single-wavelength irradiation at 254 nm using Hg-lamp, suggesting that the quantum yields are wavelength dependent. Although further investigation on such wavelength dependence is desirable, the quantum yields obtained in the present study under continuous UV-visible irradiation similar to that of solar spectra should serve as a first-order value for investigating the contribution of Fe(II) photo-oxidation reaction on early Mars.

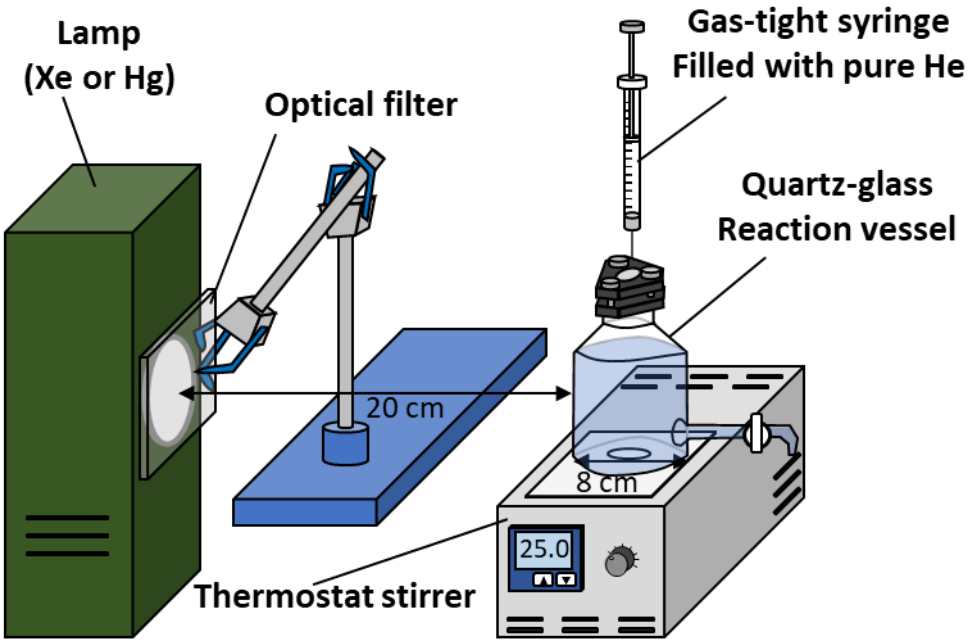

Fig. 2–1. Experimental setup. The Xe lamp was placed 20 cm from the quartz-glass reaction vessel, which was stirred continuously by a thermostat-magnetic stirrer at 25°C. The optical filter, when used, was set in front of the lamp. During irradiation, solution samples were collected continuously via the Teflon sampling cock upon injection of pure He through the butyl-rubber cap on the top.

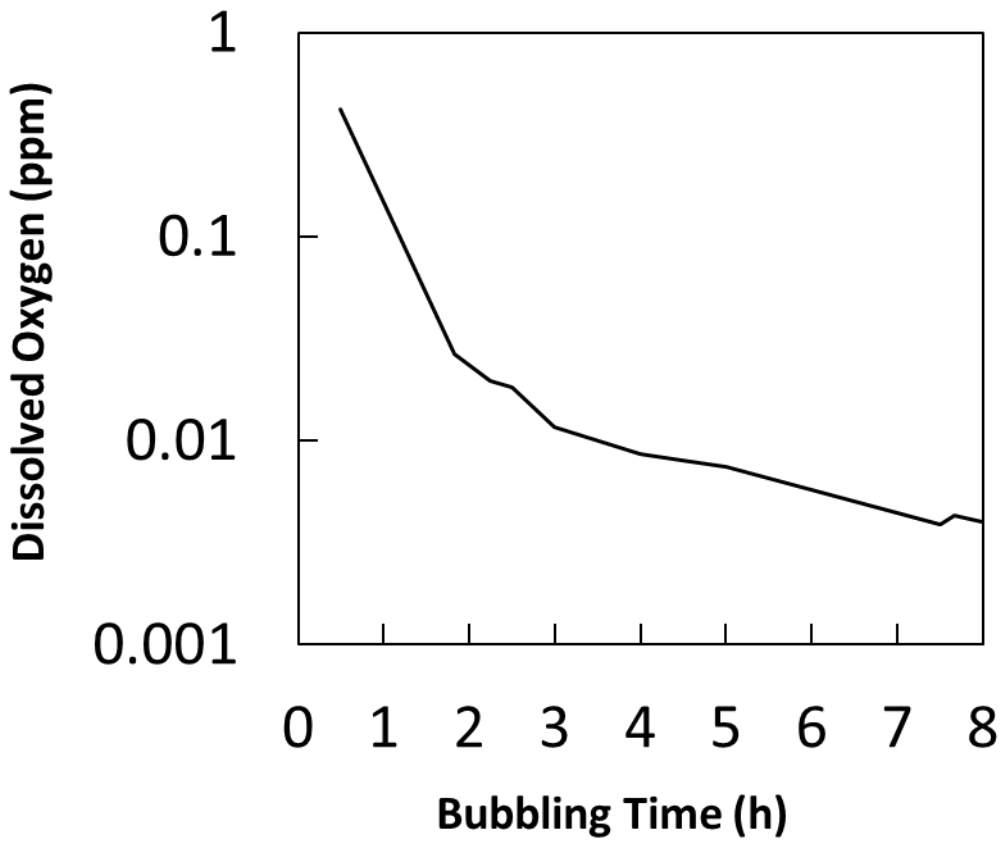

Fig. 2–2. Dissolved oxygen concentration (DO) during Ar gas bubbling. The dissolved oxygen concentration was continuously monitored during Ar gas bubbling inside the deoxygenated glovebox. The DO levels of < 0.01 ppm were achieved in ~4 hours from the start of Ar gas bubbling. Gas bubbling rate was 1.4 L min^{-1}, and pO_2 inside the glovebox during bubbling was ~10^{-15} atm.

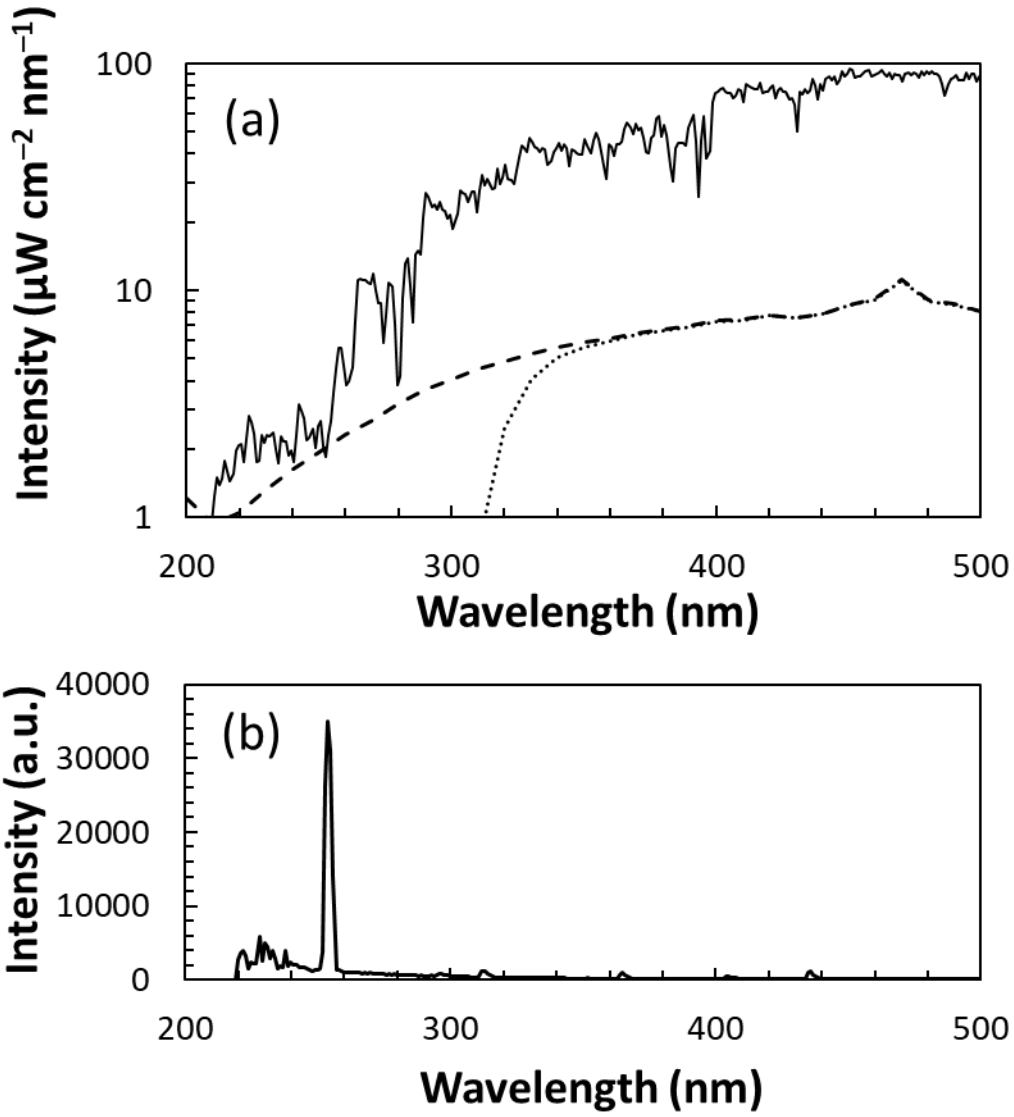

Fig. 2–3. UV and visible spectra of light sources. (a) UV and visible spectra of a Xe lamp without the optical filter and with the optical filter (dashed and dotted lines, respectively) compared with the solar spectrum (solid line). Xe-lamp irradiance and filter transmittance data were provided by the relevant manufacturer; solar irradiance data are based on the American Society for Testing and Materials air mass zero reference spectrum (ASTM E-490), corrected for distance for the average Martian semi-major axis (1.5 AU). (b) UV–visible spectra of a low-pressure Hg lamp, based on irradiance data obtained by UV–vis spectrophotometry. Although intensity is given in an arbitrary unit, relative intensities were determined from the irradiance of the Xe lamp.

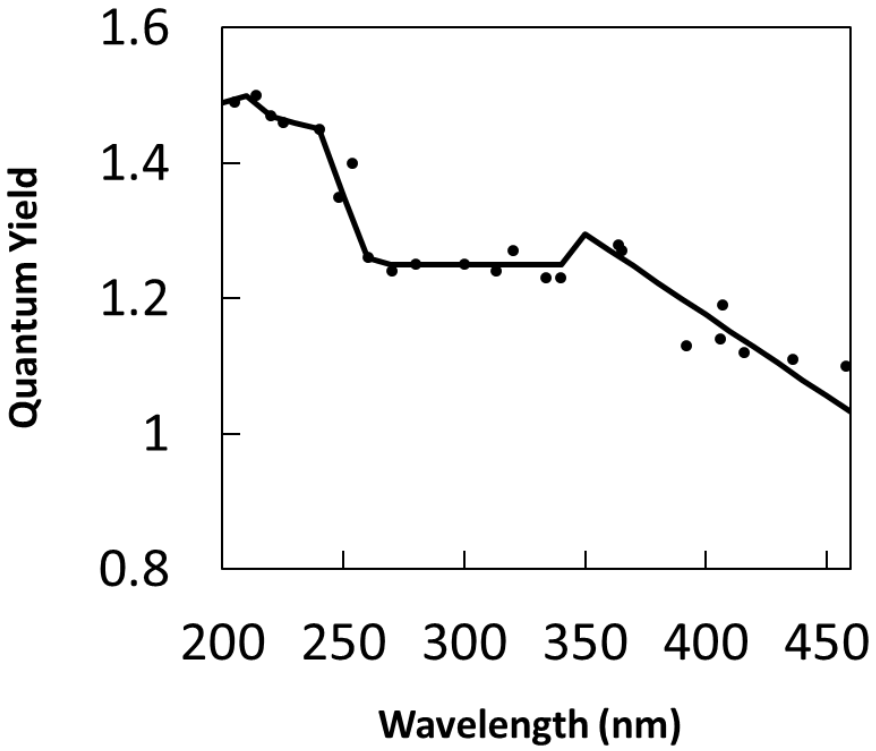

Fig. 2–4. Compiled quantum yields of potassium ferrioxalate photo-reduction at various wavelengths. The quantum yield data are from Murov (1993) and Goldstein and Rabani (2008). The thick line represents the 10-nm step values used in the calculation of photon flux.

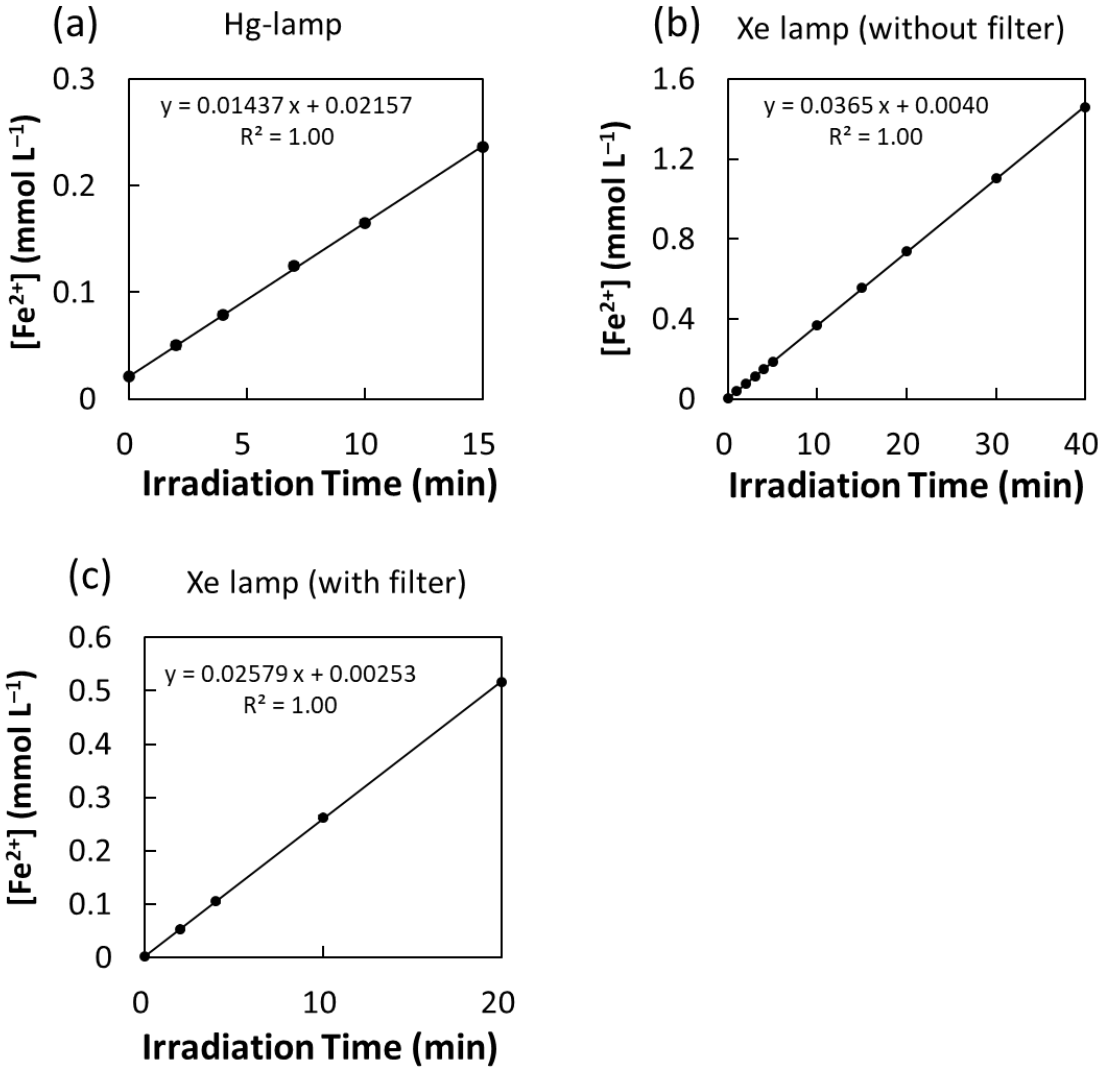

Fig. 2–5. Time trends of $[Fe^{2+}]$ during irradiation of Hg-lamp, Xe-lamp, and Xe-lamp with the filter in actinometry experiments. (a) Hg lamp; (b) Xe lamp ; (c) Xe lamp with the optical filter. The linear increase trend of $[Fe^{2+}]$ over irradiation time shows that dissolved potassium ferrioxalates are photo-reduced to ferrous ions.

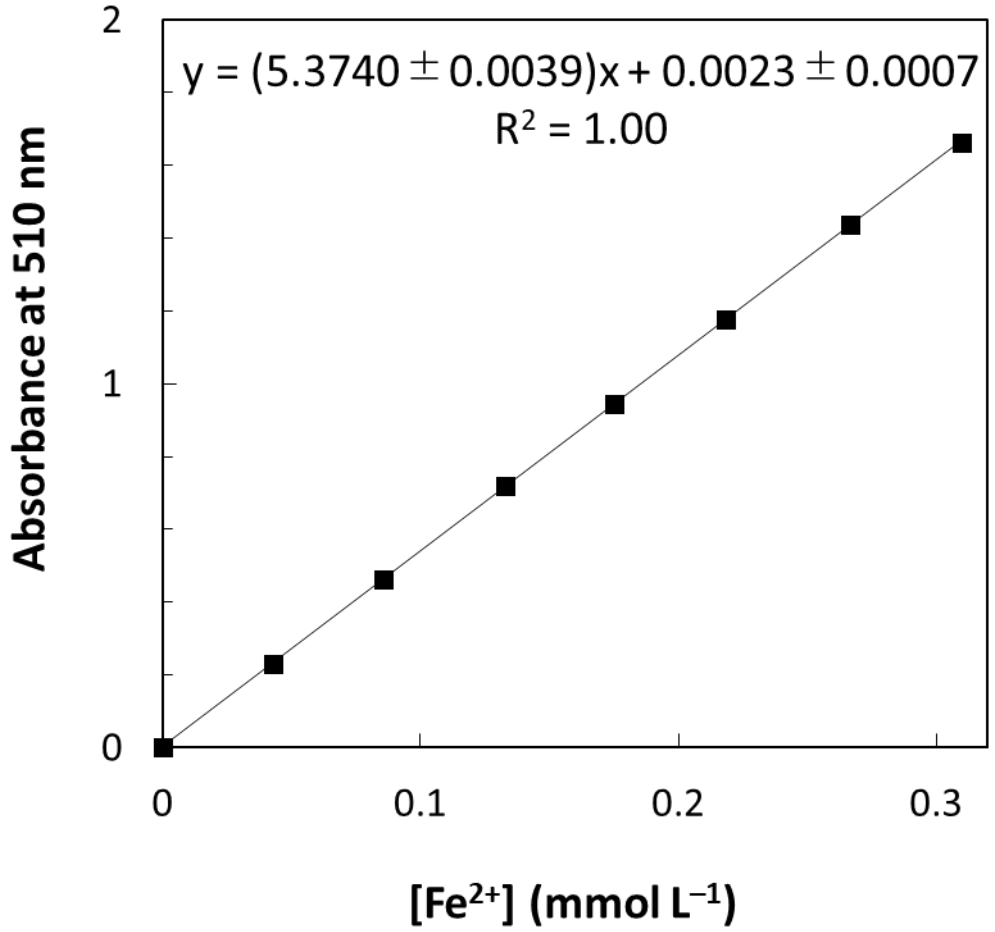

Fig. 2–6. Calibration line for measurement of [Fe^{2+}] in the phenanthroline method. The absorbance at 510 nm shows a linear relationship with [Fe^{2+}]. The fitted curve obtained by the least-square fitting is also shown.

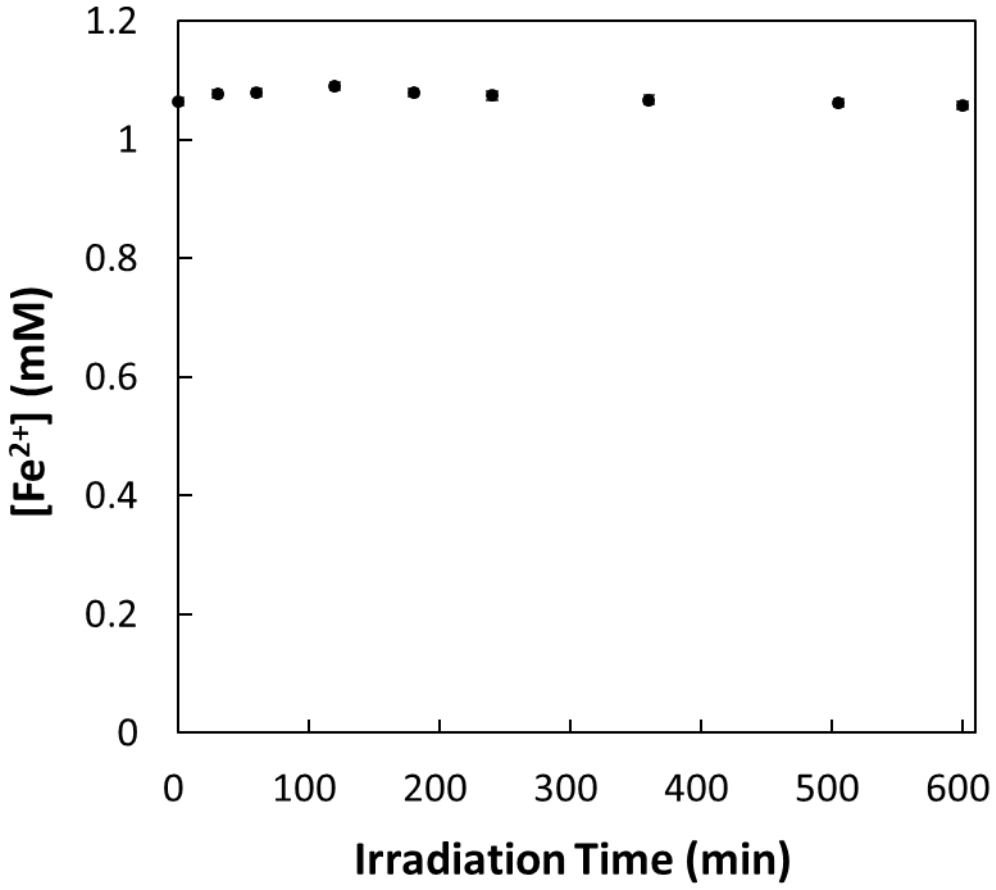

Fig. 2–7. Time trend of $[Fe^{2+}]$ in the experimental solution without irradiation (run 13). A deoxygenated experimental solution was prepared in the glovebox with initial $[Fe^{2+}]_{tot}$ = 1.06 mmol L^{-1} and pH buffered to 7.1 by Bis-Tris and HNO_3. The reaction vessel was covered with aluminum foil and kept in the dark to avoid photo-oxidation.

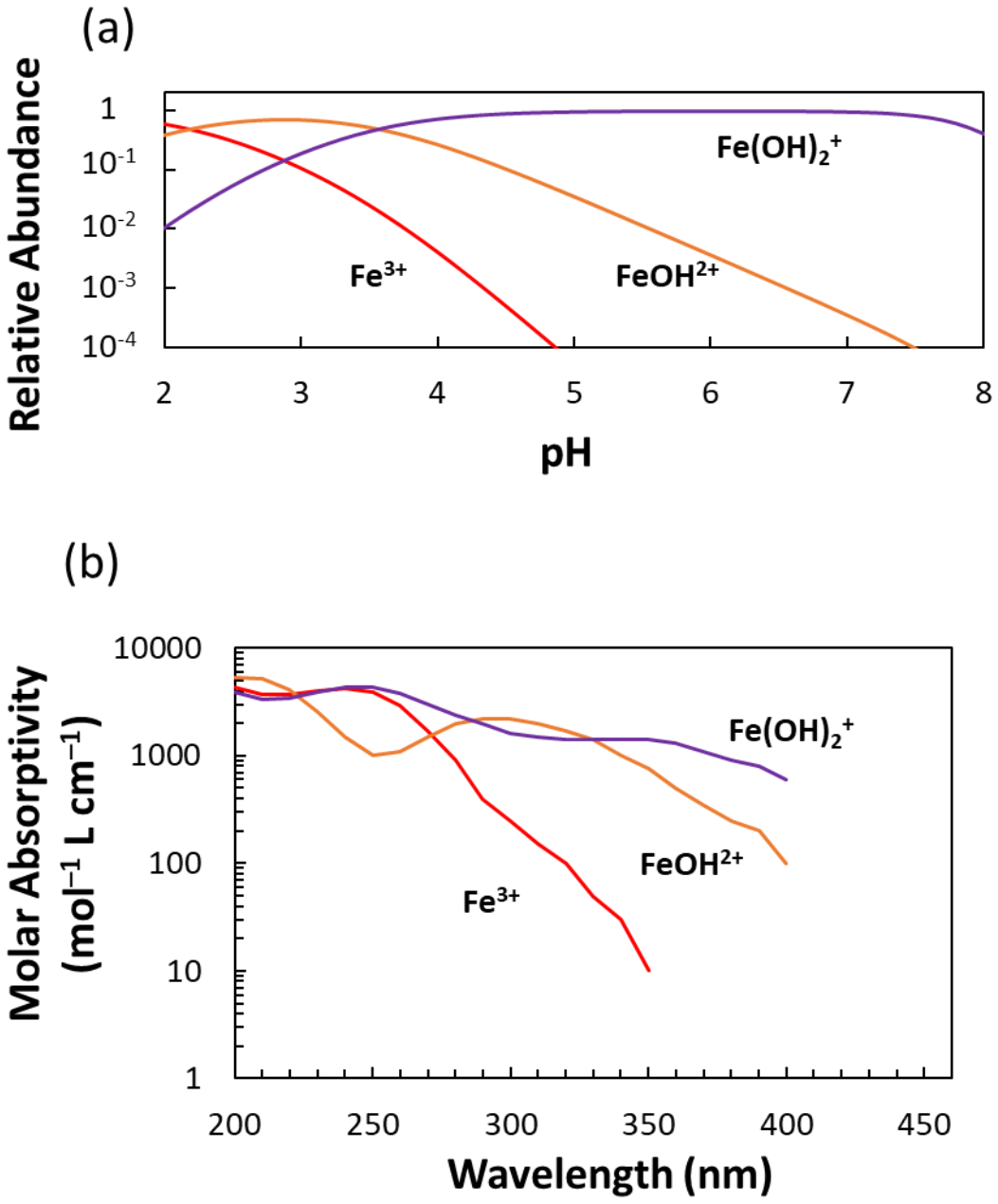

Fig. 2–8. UV absorptivity and pH dependence of Fe(III) species in solution. (a) Relative abundances (molar fractions) of aqueous and Fe (III) species as a function of pH, based on the equilibrium constants of Fe^{3+} hydrolysis reactions at 25ºC reported by Stefansson (2007). (b) Molar absorption coefficients of aqueous Fe(III) species based on absorptivity data from Stefansson (2007).

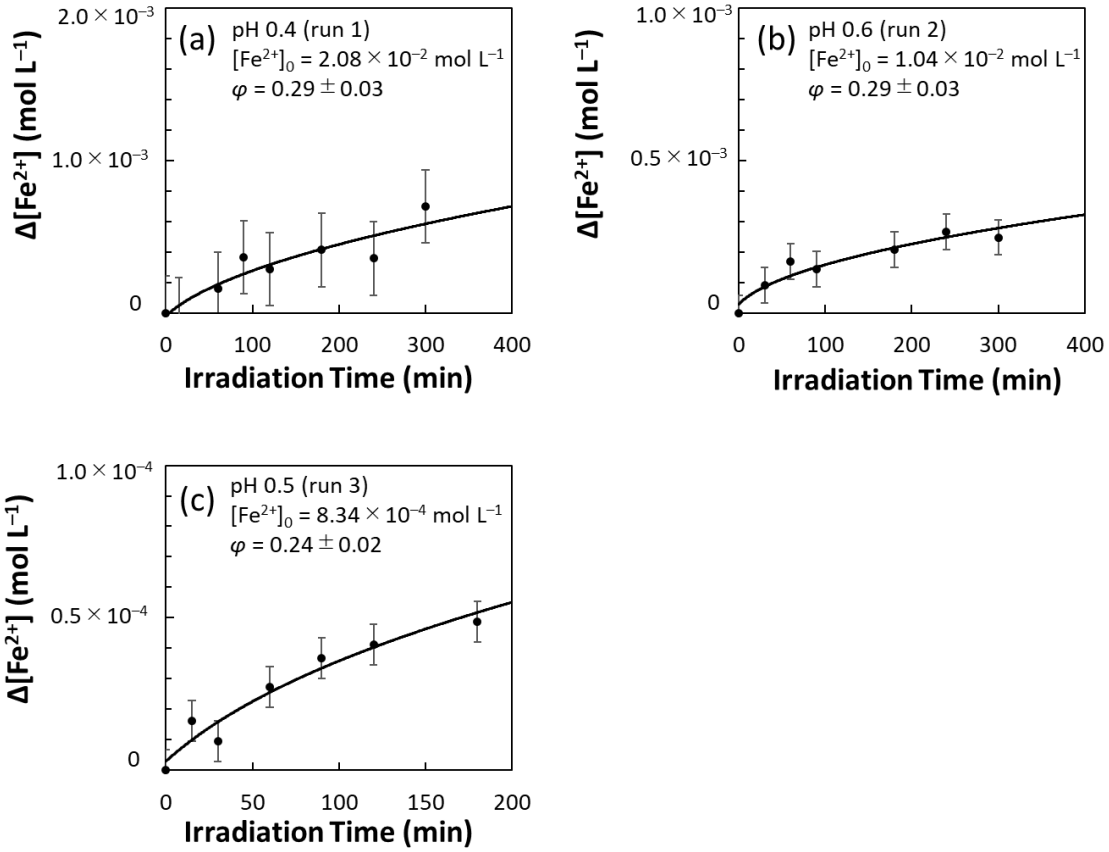

Fig. 2–9. Time trends of $\Delta[Fe^{2+}]$ during UV irradiation by the Hg lamp at different pH and initial $[Fe^{2+}]$ values. (a) pH 0.4, $[Fe^{2+}]_0 = 2.08 \times 10^{-2}$ mol L^{-1}; (b) pH 0.6, $[Fe^{2+}]_0 = 1.04 \times 10^{-2}$ mol L^{-1}; (c) pH 0.5, $[Fe^{2+}]_0 = 8.34 \times 10^{-4}$ mol L^{-1}. Estimated quantum yields, φ, are shown in each panel. Solid least-squares regression lines are shown. Run numbers refer to **Table 2–2**. $\Delta[Fe^{2+}]$ is the difference in $[Fe^{2+}]$ from the initial value ($[Fe^{2+}]_0$) after a certain time, t (min), of irradiation ($[Fe^{2+}]_t$): $\Delta[Fe^{2+}] = [Fe^{2+}]_0 - [Fe^{2+}]_t$. Error bars are 1σ.

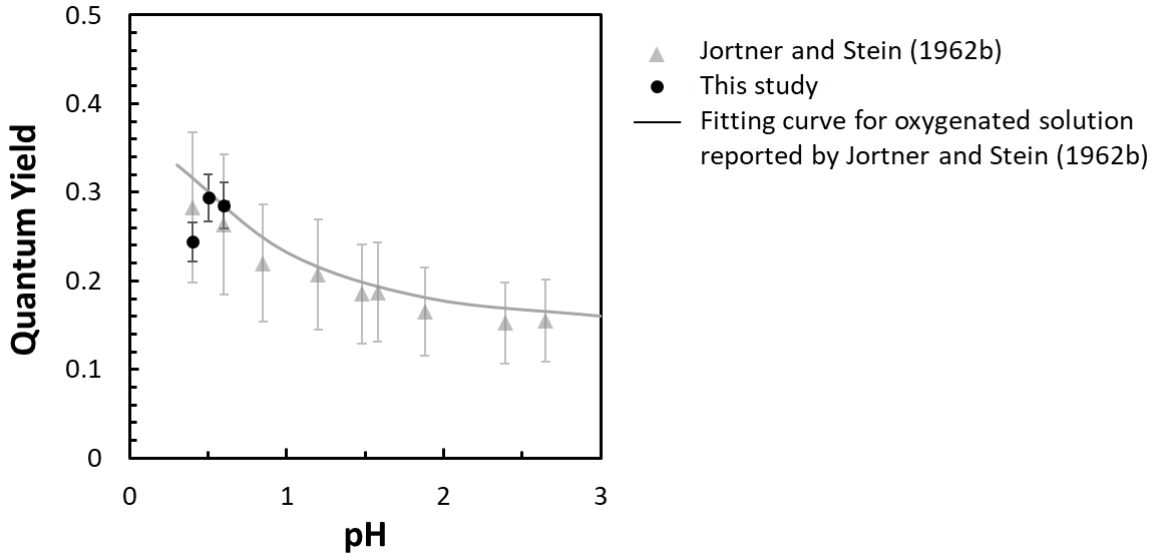

Fig. 2–10. Quantum yields of Fe^{2+} photo-oxidation under irradiation by Hg lamp plotted as a function of solution pH (black dots). Quantum yields of Fe^{2+} photo-oxidation at pH 0.4–3.0 in oxygenated solutions (gray triangles) and their pH dependence (gray curve) (Jortner and Stein, 1962b) are shown for comparison.

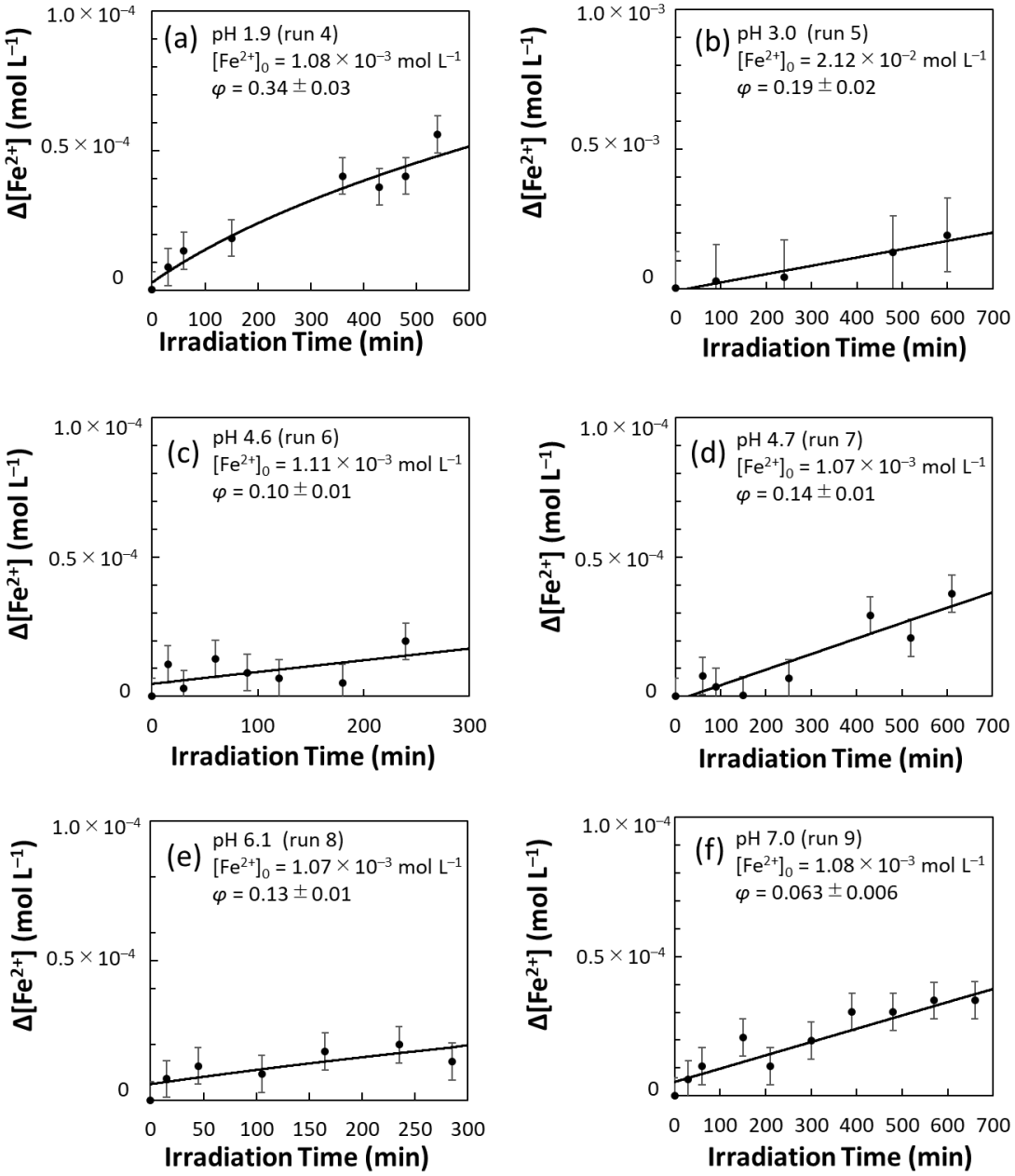

Fig. 2–11. Time trends of Δ[Fe^{2+}] during Xe-lamp irradiation. (a–f) Solution pH was 1.9, 3.0, 4.6, 4.7, 6.1, and 7.0, respectively, without the optical filter. (g–i) Solution pH was 7.1, 7.4, and 7.6, respectively, with the optical filter applied. Derived quantum yields and initial [Fe^{2+}] values are shown in each panel with least-squares regression lines. Run numbers refer to **Table 2–2**. Error bars are 1σ.

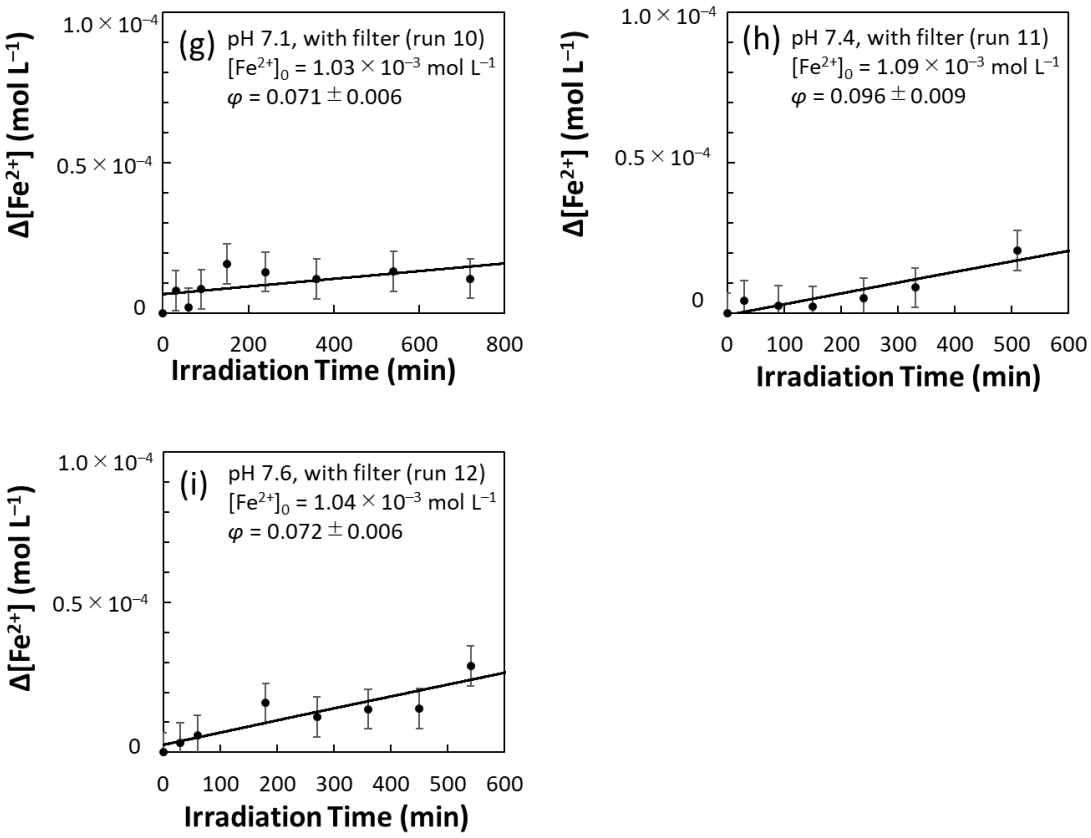

Fig. 2–11. (continued).

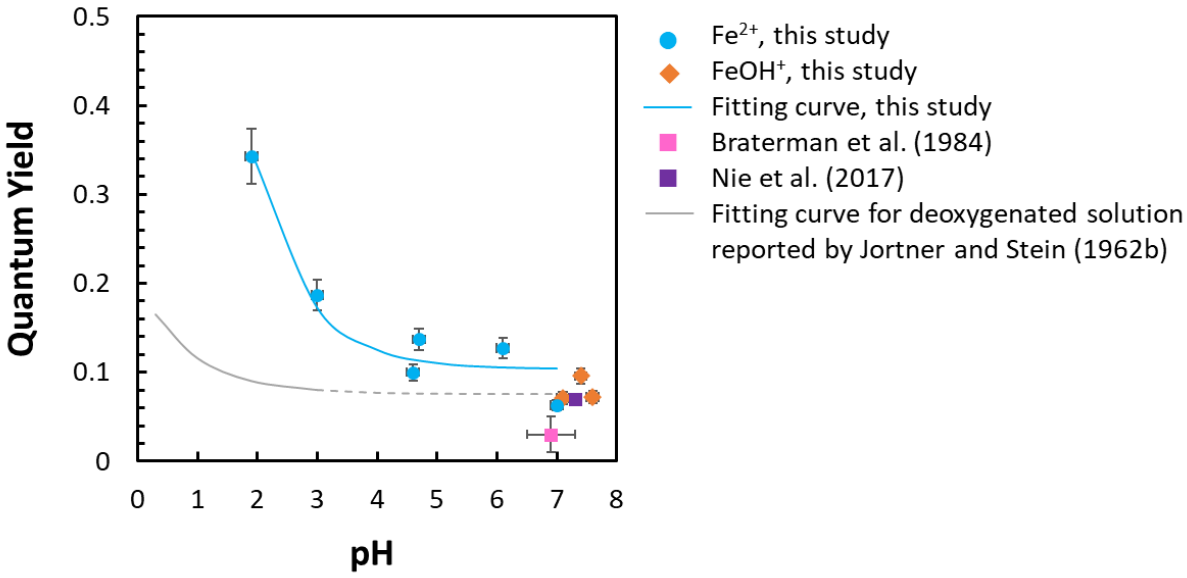

Fig. 2–12. Quantum yields of Fe^{2+} and $FeOH^{+}$ photo-oxidation under irradiation by Xe lamp plotted as a function of solution pH (cyan dots and orange diamonds, respectively). Plotted with the semi-empirical equation of the pH-dependence of quantum yield of Fe^{2+} photo-oxidation derived in this study (Eq. 2–8; cyan curve). Quantum yields of $FeOH^{+}$ photo-oxidation estimated by Braterman et al. (1984) (0.01–0.05) and Nie et al. (2017) (0.07) are shown for comparison (pink and purple squares, respectively). Solid and dashed gray curves represent the pH-dependence of quantum yield for Fe^{2+} photo-oxidation at pH 0.4–3.0 in deoxygenated solutions (Eq. 1–2; Jortner and Stein, 1962b) and its extrapolation to pH > 3.0, respectively.

Table 2–1. Measured photon fluxes in the actinometry experiments. The photon fluxes of light sources measured by the potassium ferrioxalate actinometry method are shown with initial concentrations of potassium ferrioxalate and irradiation time.

Light source	Initial [K-ferrioxalate] (mol L^{-1})	Irradiation time (min)	Photon flux (mol min^{-1} L^{-1})
Hg lamp	6.01×10^{-3}	15	$1.15 \pm 0.01 \times 10^{-5}$
Xe lamp without filter (> 200 nm)	1.53×10^{-2}	40	$3.09 \pm 0.01 \times 10^{-5}$
Xe lamp with filter (> 300 nm)	6.12×10^{-3}	20	$2.23 \pm 0.01 \times 10^{-5}$

Table 2–2. Summary of experimental conditions. The initial pH and its compositions of the experimental solutions, initial concentration of Fe(II), the light source used, and the duration of irradiation in each experimental run are summarized.

Run number	Light source	pH	Buffer composition	Initial [Fe^{2+}] (mol L^{-1})	Irradiation time (min)
1	Hg	0.5	0.4 M H_2SO_4	2.08×10^{-2}	300
2	Hg	0.6	0.4 M H_2SO_4	1.04×10^{-2}	300
3	Hg	0.4	0.4 M H_2SO_4	8.34×10^{-4}	180
4	Xe	1.9	10^{-2} M H_2SO_4	1.08×10^{-3}	540
5	Xe	3.0	10^{-3} M H_2SO_4	2.12×10^{-2}	600
6	Xe	4.6	10^{-5} M HNO_3	1.11×10^{-3}	240
7	Xe	4.7	10^{-5} M HNO_3	1.07×10^{-3}	610
8	Xe	6.1	0.029 M H_2SO_4 + 0.071 M Bis-Tris	1.07×10^{-3}	290
9	Xe	7.0	0.013 M H_2SO_4 + 0.087 M Bis-Tris	1.08×10^{-3}	660
10	Xe + filter	7.1	0.017 M HNO_3 + 0.083 M Bis-Tris	1.03×10^{-3}	720
11	Xe + filter	7.4	0.011 M HNO_3 + 0.089 M Bis-Tris	1.09×10^{-3}	510
12	Xe + filter	7.6	0.007 M HNO_3 + 0.093 M Bis-Tris	1.04×10^{-3}	540
13	No light	7.1	0.017 M HNO_3 + 0.083 M Bis-Tris	1.06×10^{-3}	600

Chapter 3. Effect of UV spectrum on photo-oxidation of ferrous iron: Implications for the trigger of acidification on Mars

本章については、5 年以内に雑誌掲載等の形で公開予定のため非公開とする。

Chapter 4. Implications for atmospheric and hydrological conditions for redox stratification on early Gale lakes

本章については、5 年以内に雑誌掲載等の形で公開予定のため非公開とする。

Chapter 5. General conclusions

本章については、5 年以内に雑誌掲載等の形で公開予定のため非公開とする。

Acknowledgments

First and foremost, I would like to express my deepest gratitude to my advisor, professor Yasuhito Sekine for his passionate guidance and kind support. Ever since I joined the Sekine lab for the undergraduate thesis, he has always been a good role model as a scientist and will continuously be. Without his support and encouragement, it would not have been possible to complete the thesis successfully.

Besides my advisor, I am also grateful to my collaborators: Prof. Seiji Sugita, Prof. Kazumi Ozaki, and Dr. Yoshiki Kanzaki, for their insightful advice and encouragement on my projects. I also wish to thank Prof. Takashi Murakami, Prof. Yoshio Takahashi, and Prof. Tsuyoshi Iizuka for their support in developing the experimental system and the use of laboratory equipment.

I would especially like to thank the members of my dissertation committee for their patience and time and the wonderful suggestions and comments I received in the defense. While on my revise of the thesis, I was delighted to look for the fundamental chemistry papers suggested by Prof. Y. Takahashi and Prof. S. Tachibana. The kind suggestions from the viewpoint of cutting-edge professionals of geology and planetary science by Prof. K. Goto and Prof. Y. Sekine were also very helpful in brushing up my thesis. Comments on the modeling techniques and the physics were the toughest but the best for a modeling beginner like me; thank you very much, Prof. E. Tajika. It was my pleasure to have such a fantastic committee.

My sincere thanks goes to Prof. E. Tajika, Prof. R. Tada, Prof. H. Nagahara, Prof. Y. Abe, Prof. H. Kayanne, Prof. M. Ikoma, Prof. S. Takahashi, Prof. N. Moteki, and Prof. H. Kawahara for constructive discussions and valuable suggestions in seminars I attended at the University of Tokyo. I also wish to thank Prof. H. Genda, Prof. T. Usui, Dr. K. Hamano, Dr. H. Kurokawa, Dr. R. Hyodo, Dr. K. Sugiura, D. Shoji, Dr. N. Zhang, and Dr. Y. Endo for fruitful discussions and helpful comments after I moved to Earth-Life Science Institute (ELSI) in Tokyo Institute of Technology.

I would also like to thank all of the graduate students I have met on the course of my Ph.D. for casual discussions over lunch or a cup of coffee and tea; some of them turned out to be critical to my studies. Thank you to Dr. E. Tatsumi, Dr. H. Kuwahara, Dr. Y. Cho, Dr. S. Kadoya, Mr. Y. Chang, Dr. M. Harada, Mr. K. Kodama, Mr. J. Kobayashi, and Mr. Y. Nakagawa, the members of the former astrobiology group at the Kashiwa Campus for kindly introducing me to the wonderful world of planetary science. Many thanks to Dr.

A. Seki, Dr. K. Kurosaki, Dr. K. Saito, Dr. Y. Suzuki, Dr. Y. Ito, Dr. Y. Kawashima, Dr. T. Kodama, Dr. A. Nakayama, Mr. S. Kurokawa, Dr. Y. Aoyama, Dr. S. Shibata, Ms. M. Ozawa, Dr. T. Tada, Mr. T. Kanzaki, Ms. K. Mitake, Mr. Y. Watanabe, Ms. M. Haga, Ms. A. Akiyama, and Mr. T. Tajiri, the members of the Earth and Planetary System Science Group, for countless enjoyable memories including student seminars (Atmosphere Seminar, Magma Ocean Seminar, and FF Seminar), open campus, System Group field camps, and more. Special thanks to those who joined the group in the same year: H. Kinjo, S. Saito, Y. Tsunazawa, Y. Uchida, N. Hasegawa, M. Mitsumoto, T. Kobayashi, T. Suwa, H. Furukawa.

I also had a great pleasure working with Prof. K. Hirose, Prof. M. Voytek, Prof. J. Hernlund, Prof. S. Ida, Prof. J. Kirschvink, Prof. S. McGlynn, Prof. K. Fujishima, Prof. H. Christine, Prof. J. Tony, Prof. M. Laneuville, Prof. T. Mochizuki, Prof. R. Brasser, Dr. H. Smith, Dr. H. Thilina, Dr. N. Guttenberg, Dr. S. Tateno, Dr. K. Johnson-Finn, Dr. I. Bonati, Ms. P. Paula, and Ms. H. Fatima at ELSI since Sekine lab moved here in 2019 June. ELSI is an excellent research institute with an at-home atmosphere and amazing diversities. It was truly a fantastic experience that I had a chance to work at ELSI on my course of Ph.D.

In recent years, a substantial part of my life was spent with members of the Sekine lab. Thank you to S. Tan, M. Yoda, Y. Luo, N. Noda, S. Imamura, M. Nakamura, T. Chida, H. Shozaki, E. Hirai, K. Kaneko, M. Sugiuchi, T. Sato, and K. Taniguchi. Although it was sometimes tough to be the most senior student for the whole years of my Ph.D., I also owe my thanks to you for being friendly and patient with my undesired advice. I wish you all the best in pursuing science in this fantastic lab and a great future.

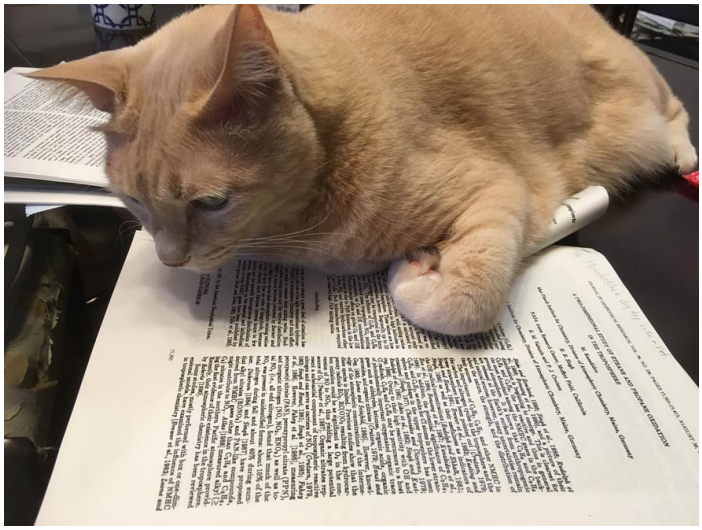

Mark

I am also very thankful to my friends who have taken me out outside the labs. Special thanks to Dr. N. Yoshioka, N. Komatsu, and the members of the Soba Tea Party (R. A., Y. H., and K. M.). I also gratefully acknowledge the financial support from the JSPS fellowship for young scientists. Finally, my sincerest thanks to my family, including our cat, Mark, for their support and encouragement.

Haruhisa Tabata

References

Anbar A. D. and Holland H. D. (1992) The photochemistry of manganese and the origin of banded iron formations. *Geochim. Cosmochim. Acta* **56**, 2595–2603.

Andrews-Hanna J. C., Phillips R. J., and Zuber M. T. (2007) Meridiani Planum and the global hydrology of Mars. *Nature*, **446**, 163–166.

Baes C. F. and Mesmer R. E. (1976) *The Hydrolysis of Cations*. John Wiley, New York.

Baker V. R. and Milton D. J. (1974) Erosion by Catastrophic Floods on Mars and Earth. *Icarus*, **23**, 27–41.

Baker V. R. (2001) Water and the martian landscape. *Nature*, **412**, 228–236.

Batalha, N., Domagal-Goldman, S. D., Ramirez, R. and Kasting, J. F. (2015) Testing the early Mars H_2–CO_2 greenhouse hypothesis with a 1-D photochemical model. *Icarus*, **258**, 337–349.

Bénézeth P., Dandurand J. L. and Harrichoury J. C. (2009) Solubility product of siderite ($FeCO_3$) as a function of temperature (25–250 °C). *Chemical Geology*, **265**, 3–12.

Bernas A., Ferradini C. and Jay-Gerin, J.-P. (1997) On the electronic structure of liquid water: Facts and reflections. *Chemical Physics*, **222**, 151–160.

Bibring J-P., Langevin Y., Mustard J. F., Poulet F., Arvidson R., Gendrin A., Gondet B., Mangold N., Pinet P., Forget F. and the OMEGA team. (2006) Global Mineralogical and Aqueous Mars History Derived from OMEGA/Mars Express Data. *Science*, **312**, 400–404.

Blake D., Vaniman D., Achilles C., Anderson R., Bish D., Bristow T., Chen C., Chipera S., Crisp J., Des Marais D., Downs R. T., Farmer J., Feldman S., Fonda M., Gailhanou M., Ma H., Ming D. W., Morris R. V., Sarrazin P., Stolper E., Treiman A. and Yen A. (2012) Characterization and Calibration of the CheMin Mineralogical Instrument on Mars Science Laboratory. *Space Science Reviews,* **170**, 341–399.

Boudreau, B. P., Middelburg, J. J. and Luo, Y. (2018) The role of calcification in carbonate compensation. *Nature Geoscience*, **11**, 894–900.

Braterman P. S., Cairns-Smith A. G. and Sloper R. W. (1983) Photo-oxidation of hydrated Fe^{2+}—significance for banded iron formations. *Nature* **303**, 163–164.

Braterman P. S., Cairns-Smith A. G., Sloper R. W., Truscott T. G. and Craw M. (1984) Photo-oxidation of Iron(II) in Water between pH 7.5 and 4.0. *J. Chem. Soc. Dalton Trans.* **7**, 1441–1445.

Bristow T. F., Haberle R. M. and Blake D. F. (2017) Low Hesperian P_{CO2} constrained from in situ mineralogical analysis at Gale Crater, Mars. *Proc. Natl. Acad. Sci.* **114**, 2166–2170.

Burkholder, J. B., Sander, S. P., Abbatt, J. P. D., Barker, J. R., Huie, R. E., Kolb, C. E., Kurylo, M. J., Orkin, V. L., Wilmouth, D. M. and Wine, P. H. (2015) Chemical kinetics and photochemical data for use in atmospheric studies: evaluation number 18. JPL Publication 15–10, Jet Propulsion Laboratory, Pasadena.

Cabrol N. A. and Grin E. A. (1999) Distribution, Classification, and Ages of Martian Impact Crater Lakes. *Icarus*, **142**, 160–172.

Catling, D. and Kasting, J. (2017) Atmospheric Evolution on Inhabited and Lifeless Worlds. Cambridge: Cambridge University Press.

Chevrier V., Rochette, P., Mathé P. E. and Grauby O. (2004) Weathering of iron-rich phases in simulated Martian atmospheres, *Geology*, **32**, 1033–1036.

Chevrier V., Poulet F., and Bibring J.-P. (2006) Early geochemical environment of Mars as determined from thermodynamics of phyllosilicates. *Nature*, **448**, 60–63.

Christensen P. R., Bandfield J. L., Hamilton V. E., Ruff S. W., Kieffer, H. H., Titus T. N., Malin M. C., Morris R. V., Lane M. D., Clark R. L., Jakosky B. M., Mellon M. T., Pearl J. C., Conrath B. J., Smith M. D., Clancy R. T., Kuzmin, R. O., Roush T., Mehall G. L., Gorelick N., Bender K., Murray K., Dason S., Greene E., Silverman S. and Greenfield M. (2001) Mars Global Surveyor Thermal Emission Spectrometer experiment: Investigation description and surface science result. *Journal of Geophysical Research*, **106**, E10. 23823–23871.

Churchill, J. H. and Csanady, G. T. (1983) Near-surface measurements of quasi-Lagrangian velocities in open water, *Journal of Physical Oceanography*, **13**(9), 1669–1680.

Claire M. W., Sheets J., Cohen M., Ribas I., Meadows V. S. and Catling D. C. (2012) The evolution of solar flux from 0.1 nm to 150 μm: quantitative estimates for planetary studies. *Astrophy. J.* **757**:95.

Dehouck E., Chevrier V., Gaudin A., Mangold N., Mathé.P.-E. and Rochette P. (2012) Evaluating the role of sulfide-weathering in the formation of sulfates or carbonates on Mars. *Geochimica et Cosmochimica Acta*, **90**, 47–63.

Dehouck E., Gaudin A., Mangold N., Lajaunie L., Dauzères A., Grauby O. and Le Menn E. (2014) Weathering of olivine under CO_2 atmosphere: A martian perspective. *Geochimica et Cosmochimica Acta,* **135**, 170–189.

Dehouck E., Gaudin A., Chevrier V. and Mangold N. (2016) Mineralogical record of the redox conditions on early Mars. *Icarus*, **271**, 67–75.

Ehlmann B. L., Mustard J. F., Swayze G. A., Clark R. N., Bishop J. L., Poulet F., Des Marais D. J., Roach L. H., Milliken R. E., Wray J. J., Barnouin-Jha O. and Murchie S. L. (2009) Identification of hydrated silicate minerals on Mars using MRO-CRISM: Geologic context near Nili Fossae and implications for aqueous alteration. *J. Geophys. Res.*, **114**, E00D08.

Ehlmann B. L., Mustard J. F., Murchie S. L., Bibring J.-P., Meunier A., Fraeman A. A. and Langevin Y. (2011) Subsurface water and clay mineral formation during the early history of Mars, *Nature* **479**, 53–60.

Ehlmann B. L. and Edwards C. S. (2014) Mineralogy of the Martian Surface, *Annu Rev Earth Planet Sci*, **42**, 291–315.

Ehlmann B. L., Anderson F. S., Andrews-Hanna J., Catling D. C., Christensen P. R., Cohen B. A., Dressing C. D., Edwards C. S., Elkins-Tanton L. T., Farley K. A., Fassett C. I., Fischer W. W., Fraeman A. A., Golombek M. P., Hamilton V. E., Hayes A. G., Herd C. D. K., Horgan B., Hu R., Jakosky B. M., Johnson J. R., Kasting J. F., Kerber L., Kinch K. M., Kite E. S., Knutson H. A., Lunine J. I., Mahaffy P. R., Mangold N., McCubbin F. M., Mustard J. F., Niles P. B., Quantin-Nataf C., Rice M. S., Stack K. M., Stevenson D. J., Stewart S. T., Toplis M. J., Usui T., Weiss B. P., Werner S. C., Wordsworth R. D., Wray J. J., Yingst R. A., Yung Y. L. and Zahnle K. J. (2016). The sustainability of habitability on terrestrial planets: Insights, questions, and needed measurements from Mars for understanding the evolution of Earth-like worlds. *J. Geophys. Res.Planets*, **121**, 1927–1961.

Ehrenfreund M. and Leibenguth J.-L. (1970) Étude des équilibres d'hydolyse des ions de Fe(II) par spectrohotométrie ultra-violette et visible. II. – Étude en milieu $(NH_4)_2SO_4$, - 2M, ou $NaClO_4$ -2M. Essai d'interpretation. *Bulletin de la Société Chimique de France* **7**, 2498–2505.

Farrand W. H., Glotch T. D., Rice Jr. J. W., Hurowitz J. A. and Swayze G. A. (2009) Discovery of jarosite within the Mawrth Vallis region of Mars: Implications for the geologic history of the region. *Icarus*, **204**, 478–488.

Fassett C. I. and Head III J. W. (2008) Valley network-fed, open-basin lakes on Mars: Distribution and implications for Noachian surface and subsurface hydrology. *Icarus*, **198**, 37–56.

Fewell M. P. and Trojan A. v. (2019) Absorption of light by water in the region of high transparency: recommended values for photon-transport calculations, *Applied Optics* **58(9)**, 2408–2421.

Forget, F. and Pierrehumbert, R. T. (1997) Warming Early Mars with Carbon Dioxide Clouds That Scatter Infrared Radiation. *Science* **278**, 1273–1276.

Forsythe R. D. and Blackwelder C. R. (1998) Closed drainage crater basins of the Martian highlands: Constraints on the early Martian hydrologic cycle. *Journal of Geophysical Research*, **103**, E13. 31421–31431.

Fraeman, A. A., Edgar, L. A., Rampe, E. B., Thompson, L. M., Frydenvang, J.,Fedo, C. M., Catalano J. G., Dietrich W. E., Gabriel T. S. J., Vasavada A. R., Grotzinger J. P., L'Haridon J., Mangold N., Sun V. Z., House C. H., Bryk A. B., Hardgrove C., Czarnecki S., Stack K. M., Morris R. V., Arvidson R. E., Banham S. G., Bennett K. A., Bridges J. C., Edwards C. S., Fischer W. W., Fox V. K., Gupta S., Horgan B. H. N., Jacob S. R., Johnson J. R., Johnson S. S., Rubin D. M., Salvatore M. R., Schwenzer S. P., Siebach K. L., Stein N. T., Turner S. M. R., Wellington D. F., Wiens R. C., Williams A. J., David G. and Wong G. M. (2020). Evidence for a diagenetic origin of Vera Rubin ridge, Gale crater, Mars: Summary and synthesis of Curiosity's exploration campaign. *Journal of Geophysical Research: Planets*, **125**, e2020JE006527.

Fukushi K., Sekine Y., Sakuma H., Morida K. and Wordsworth R. (2019) Semiarid climate and hyposaline lake on early Mars inferred from reconstructed water chemistry at Gale. *Nature Communications* **10**, 4896.

Gasda P. J., Das D., Nellessen M., Dehouck E., Rapin W., Meslin P.-Y., Newsom H., Baker A., Hoffman M., Ganter G., Fey D., Kronyak R., Frydenvang J., Wiens R. C., Clegg S., Maurice S. and Gasnault O. (2020) Veins in Glen Torridon, Gale Crater, Mars: Exploring the Potential Transition into the Sulfate-Bearing Unit. *Lunar and Planetary Science Conference LI*, abstract #1641.

Goldstein S. and Rabani J. (2008) The ferrioxalate and iodide–iodate actinometers in the UV region. *Jour. of Photochem. and Photobio. A: Chem.* **193**, 50–55.

Golombek M., Grant J., Kipp D., Vasavada A., Kirk R., Fergason R., Bellutta P., Calef F., Larsen K., Katayama Y., Huertas A., Beyer R., Chen A., Parker T., Pollard B., Lee S., Sun Y., Hoover R., Sladek H., Grotzinger J., Welch R., Noe Dobrea E., Michalski J. and Watkins M. (2012) Selection of the Mars Science Laboratory Landing Site. *Space Sci Rev*, **170**, 641–737.

Grant J. A., Wilson S. A., Mangold N., Calef III F. and Grotzinger J. P. (2014) The timing of alluvial activity in Gale crater, Mars, *Geophys. Res. Lett.*, **41**, 1142–1148.

Grotzinger J. P. and Milliken R. E. (2012) The sedimentary rock record of Mars: Distribution, origins, and global stratigraphy, in Sedimentary Geology of Mars. (SEPM Special Publication, Tulsa, OK, 2012), vol. 102.

Grotzinger J. P., Sumner D. Y., Kah C., Stack K., Gupta S., Edgar L., Rubin D., Lewis K., Schieber J., Mangold N., Milliken R., Conrad P. G., DesMarais D., Farmer J.,

Siebach K., Calef III F., Hurowitz J., McLennan S. M., Ming D., Vaniman D., Crisp J., Vasavada A., Edgett K. S., Malin M., Blake D., Gellert R., Mahaffy P., Wiens R. C., Maurice S., Grant J. A., Wilson S., Anderson R. C., Beegle L., Arvidson R., Hallet B., Sletten R. S., Rice M., Bell III J., Griffes J., Ehlmann B., Anderson R. B. Bristow T. F., Dietrich W. E., Dromart G., Eigenbrode J., Fraeman A., Hardgrove C., Herkenhoff K., Jandura L., Kocurek G., Lee S., Leshin L. A., Leveille R., Limonadi D., Maki J., McCloskey S., Meyer M., Minitti M., Newsom H., Oehler D., Okon A., Palucis M., Parker T., Rowland S., Schmidt M., Squyres S., Steele A., Stolper E., Summons R., Treiman A., Williams R., Yingst A. and MSL Science Team. (2014) A Habitable Fluvio-Lacustrine Environment at Yellowknife Bay, Gale Crater, Mars. *Science*, **343**, 1242777.

Grotzinger J. P., Gupta S., Malin M. C., Rubin D. M., Schieber J., Siebach K., Sumner D. Y., Stack K. M., Vasavada A. R., Arvidson R. E., Calef III, F., Edgar L., Fischer W. F., Grant J. A., Griffes J., Kah L. C., Lamb M. P., Lewis K. W., Mangold N., Minitti M. E., Palucis M., Rice M., Williams R. M. E., Yingst R. A., Blake D., Blaney D., Conrad P., Crisp J., Dietrich W. E., Dromart G., Edgett K. S., Ewing R. C., Gellert R., Hurowitz J. A., Kocurek G., Mahaffy P., McBride M. J., McLennan S. M., Mischna M., Ming D., Milliken R., Newsom H., Oehler D., Parker T. J., Vaniman D., Wiens R. C. and Wilson S. A. (2015) Deposition, exhumation, and paleoclimate of an ancient lake deposit, Gale Crater, Mars. *Science* **350**, aac7575.

Haberle, R.M., Clancy, R.T., Forget, F., Smith, M.D. and Zurek, R.W. (2017) The Atmosphere and Climate of Mars, chapter 13, Cambridge University Press, pp.405–432.

Halevy, I. and Head III, J.W., (2014) Episodic warming of early Mars by punctuated volcanism. *Nature Geoscience*, **7**, 865–868.

Hatchard C. G. and Parker C. A. (1956) A new sensitive chemical actinometer II. Potassium ferrioxalate as a standard chemical actinometer. *Proc. of The Royal Soc. A* **235**, 518–536.

Heinrich C. A. and Seward T. M. (1990) A spectrophotometric study of aqueous iron (II) chloride complexing from 25 to 200°C. *Geochim. Cosmochim. Acta* **54**, 2207–2221.

Henderson-Sellers, B. (1988) The dependence of surface velocity in water bodies on wind velocity and latitude, *Applied Mathematical Modelling*, **12** (2), 202–203.

Horvath, O. and Papp, S. (1985) Photo-oxidation of copper(I) chloro complexes: Individual quantum yields of $[CuCl_2]^-$ and $[CuCl_2]^{-2}$, *Journal of Photochemistry*, **30**(1), 47–61.

Hoke M. R. T. and Hynek B. M. (2009) Roaming zones of precipitation on ancient Mars as recorded in valley networks, *J. Geophys. Res*., **114**, E08002.

Howard A. D., Moore J. M. and Irwin III R. P. (2005) An intense terminal epoch of widespread fluvial activity on early Mars: 1. Valley network incision and associated deposits. *J. Geophys. Res*., **110**, E12S14.

Hurowitz J. A., Fischer W. W., Tosca N. J. and Milliken R. E. (2010) Origin of acidic surface waters and the evolution of atmospheric chemistry on early Mars. *Nature Geoscience* **3**, 323–326.

Hurowitz J. A., Grotzinger J. P., Fischer W. W., McLennan S. M., Milliken R. E., Stein N., Vasavada A. R., Blake D. F., Dehouck E., Eigenbrode J. L., Fairén A. G., Frydenvang J., Gellert R., Grant J. A., Gupta S., Herkenhoff K. E., Ming D. W., Rampe E. B., Schmidt M. E., Siebach K. L., Stack-Morgan K., Sumner D. Y. and Wiens R. C. (2017) Redox stratification of an ancient lake in Gale Crater, Mars. *Science* **356**, eaah6849.

Irwin III R. P., Maxwell T. A., Howard A. D., Craddock R. A. and Leverington D. W. (2002) A Large Paleolake Basin at the Head of Ma'adim Vallis, Mars. *Science*, **296**, 2209–2212.

Ityaksov D., Linnartz H., and Ubachs W. (2008) Deep-UV absorption and Rayleigh scattering of carbon dioxide. *Chemical Physics Letters*, **462**, 31–34.

Jakosky B. (2021) Atmospheric Loss to Space and History of Water on Mars. *Annu. Rev. Earth Planet. Sci.,* **49**, 71–93.

Johnson S. S., Pavlov A. A., and Mischna M. A. (2009) Fate of SO_2 in the ancient Martian atmosphere: Implications for transient greenhouse warming. *Geophys. Res.*, **114**, E11011.

Jortner J. and Stein G. (1962a) The photochemical evolution of hydrogen from aqueous solutions of ferrous ions. Part I. The reaction mechanism at low pH. *The Jour. of Physical Chem.* **66**, 1258–1264.

Jortner J. and Stein G. (1962b) The photochemical evolution of hydrogen from aqueous solutions of ferrous ions. Part II. Effect of changing pH. *The Jour. of Physical Chem.* **66**, 1264–1271.

Kanzaki Y. and Murakami T. (2013) Rate law of Fe(II) oxidation under low O_2 conditions. *Geochim. Cosmochim. Acta* **123**, 338–350.

Kanzaki Y. and Murakami T. (2019) Rates and stoichiometry of pyrite dissolution at pH 3 under low O_2 conditions. *Chem. Geol.* **522**, 240–259.

Kerber L., Forget F., and Wordsworth R. (2015) Sulfur in the early martian atmosphere revisited: Experiments with a 3-D Global Climate Model. *Icarus*, **261**, 133–148.

Kitamura R., Pilon L. and Jonasz M. (2007) Optical constants of silica glass from extreme ultraviolet to far infrared at near room temperature. *Applied Optics*, **46**, 8118–8133.

Kite E. S., Gao P., Goldblatt C., Mischna M. A., Mayer D. P. and Yung Y. L. (2017) Methane bursts as a trigger for intermittent lake-forming climates on post-Noachian Mars. *Nature Geoscience*, **10**, 737–740.

Kite E. S. and Melwani Daswani M. (2019) Geochemistry constrains global hydrology on Early Mars. *Earth and Planet. Sci. Let.* **524**, 115718.

Klingelhöfer G., Morris R. V., Bernhardt B., Schröder C., Rodionov D. S., de Souza Jr. P. A., Yen A., Gellert R., Evlanov E. N., Zubkov B., Foh J., Bonnes U., Kankeleit E., Gütlich P., Ming D. W., Renz F., Wdowiak T., Squyres S. W. and Arvidson R. E. (2004) Jarosite and Hematite at Meridiani Planum from Opportunity's Mössbauer Spectrometer. *Science*, **306**, 1740-1745.

Knoll A. H., Carr M., Clark B., Des Marais D. J., Farmer J. D., Fishcer W. W., Grotzinger J. P., McLennan S. M., Malin M., Schröder C., Squyres S., Tosca N. J. and Wdowiak T. (2005) An astrobiological perspective on Meridiani Planum. *Earth and Planet. Sci. Let.* **240**, 179–189.

Konhauser K., Amskold L., Lalonde S. V., Posth N. R., Kappler A. and Anbar A. Decoupling photochemical Fe(II) oxidation from shallow-water BIF deposition. (2007) *Earth and Planet. Sci. Let.* **258**, 87–100.

Kuhn H. J., Braslavsky S. E. and Schmidt R. (2004) Chemical Actinometry (IUPAC Technical Report). *Pure Appl. Chem.* **76**, 2105–2146.

Lanza N. L., Wiens R. C., Arvidson R. E., Clark B. C., Fischer W. W., Gellert R., Grotzinger J. P., Hurowitz J. A., McLennan S. M., Morris R. V., Rice M. S., Bell J. F. III, Berger J. A., Blaney D. L., Bridges N. T., Calef F. III, Campbell J. L., Clegg S. M., Cousin A., Edgett K. S., Fabre C., Fisk M. R., Forni O., Frydenvang J., Hardy K. R., Hardgrove C., Johnson, J. R., Lasue J., Le Mouélic S., Malin M. C., Mangold N., Martìn-Torres J., Maurice S., McBride M. J., Ming D. W., Newsom H. E., Ollila A. M., Sautter V., Schröder S., Thompson L. M., Treiman A. H., Van Bommel S., Vaniman D. T. and Zorzano M.-P. (2016) Oxidation of manganese in an ancient aquifer, Kimberley formation, Gale crater, Mars. *Geophys. Res. Lett.* **43**, 7398–7407.

Lemire R. J., Berner U., Musikas D. A., Taylor P. P. and Tochiyama O. (2013) Chemical thermodynamics of iron - Part 1 - Chemical thermodynamics volume 13a, Nuclear Energy Agency of the OECD, OECD Publications, Paris, France.

Logan S. R. (1990) Effects of temperature and wavelength on the primary process in the photo-oxidation of iron(II) ion. *J. Chem. Soc. Faraday Trans*. **86**(4), 615–617.

Lorand J. P., Chevrier V., and Sautter V. (2005) Sulfide mineralogy and redox conditions in some shergottites. *Meteoritics and Planetary Science*, **40**, 1257–1272.

Mahaffy P. R., Webster C. R., Atreya S. K., Franz H., Wong M., Conrad P. G., Harpold D., Jones J. J, Leshin L. A., Manning H., Owen T., Pepin R. O., Squyres S., Trainer M. and MSL Science Team. (2013) Abundance and Isotopic Composition of Gases in the Martian Atmosphere from the Curiosity Rover, *Science*, **341**, 263–266.

Malin M. C. and Carr M. H. (1999) Groundwater formation of martian valleys. *Nature*, **397**, 589–591.

Manatt S. L. and Lane A. L. (1993) A compilation of the absorption cross-sections of SO2 from 106 to 403 nm. *Journal of Quantitative Spectroscopy and Radiative Transfer,* **50**(3), 267–276.

Mangold N., Kite E. S., Kleinhans M. G., Newsom H., Ansan V., Hauber E., Kraal E., Quantin C. and Tanaka, K. (2012) The origin and timing of fluvial activity at Eberswalde crater, Mars. *Icarus*, **220** (2), 530–551.

McKay C. P., Pollack J. B. and Courtin R. (1991) The greenhouse and antigreenhouse effects on Titan. *Science*, **253**, 1119–1121.

McLennan S. M., Bell J. F., Calvin W. M., Christensen P. R., Clark B. C., de Souza Jr., P. A., Farmer J., Farrand W. H., Fike D. A., Gellert R., Ghosh A., Glotch T. D., Grotzinger J. P., Hahn B., Herkenhoff K. E., Hurowitz J. A., Johnson J. R., Johnson S. S., Jolliff B., Klingelhöfer G., Knoll A. H., Learner Z., Malin M. C., McSween Jr., H. Y., Pocock J., Ruff S. W., Soderblom L. A., Squyres S. W., Tosca N. J., Watters W. A., Wyatt M. B. and Yen A. (2005) Provenance and diagenesis of the evaporite-bearing Burns formation, Meridiani Planum, Mars. *Earth and Planet. Sci. Let*. **240**, 95–121.

McLennan S. M., Grotzinger J. P., Hurowitz J. A. and Tosca N. J. (2019) The Sedimentary Cycle on Early Mars. *Annual Review of Earth and Planetary Sciences*. **47**, 91–118.

Metz J. M., Grotzinger J. P., Mohrig D., Milliken R., Prather B., Pirmez C., McEwen A. S. and Weitz C. M. (2009) Sublacustrine depositional fans in southwest Melas Chasma. *Journal of Geophysical Research*, **114**, E10002.

Millero F. J. and Roy R. N. (1997) A Chemical Equilibrium Model for the Carbonate System in Natural Waters. A chemical equilibrium model for the carbonate system, in natural waters. *Croat. Chem. Acta*, **70**, 1–38.

Milliken R. E., Swayze G. A., Arvidson R. E., Bishop J. L., Clark R. N., Ehlmann B. L., Green R. O., Grotzinger J. P., Morris R. V., Murchie S. L., Mustard J. F. and Weitz C. (2008) Opaline silica in young deposits on Mars. *Geology*, **36**, 847–850.

Milliken R. E., Grotzinger J. P. and Thomson B. J. (2010) Paleoclimate of Mars as captured by the stratigraphic record in Gale Crater. *Geophysical Research Letters*, **37**, L04201.

Mitra K. and Catalano J. G. (2019) Chlorate as a potential oxidant on Mars: rates and products of dissolved Fe(II) oxidation. *J. Geophys. Res. Planets* **124**, 2893–2916.

Mitra K., Moreland E. L. and Catalano J. G. (2020) Capacity of chlorate to oxidize ferrous iron: Implications for iron oxide formation on Mars. *Minerals* **10** (9), 729, 1–19.

Morel, A. and Bricaud, A. (1981) Theoretical results concerning light absorption in a discrete medium, and application to specific absorption of phytoplankton, *Deep Sea Research Part A. Oceanographic Research Papers*, **28** (11), 1375–1393.

Murov S. L. (1993) *Handbook of Photochemistry*, Marcel Dekker Inc., New York.

Nie N. X., Dauphas N. and Greenwood C. (2017) Iron and oxygen isotope fractionation during iron UV photo-oxidation: Implications for early Earth and Mars, *Earth and Planet. Sci. Let.* **458**, 179–191.

Nikogosyan D. N., Oraevsky A. A., and Rupasov V. I. (1983) Two-photon ionization and dissociation of liquid water by powerful laser UV radiation, *Chem. Phys.*, **77**, 131–143.

Noda N., Imamura S., Sekine Y. Kurisu M., Fukushi K., Terada N., Uesugi S., Numako C., Takahashi Y. and Hartmann J. (2019) Highly oxidizing aqueous environments on early Mars inferred from scavenging pattern of trace metals on manganese oxides. *J. Geophys. Res. Planets* **124**, 1282–1295.

Noyes, R. M. (1955) Kinetics of Competitive Processes when Reactive Fragments are Produced in Pairs, *J. Am. Chem. Soc.*, **77**(8), 2042–2045.

Oguz T., Tugrul S., Kideys A. E., Ediger V. and Kubilay N. (2005) Physical and Biogeochemical Characteristic of the Black Sea. The Sea, vol. 14, chap. 33, 1331–1369.

Osterloo M., Anderson F. S., Hamilton V. E. and Hynek B. M. (2010) Geologic context of proposed chloride-bearing materials on Mars. *Journal of Geophysical Research*, **115**, E100012.

Osterloo M. M., Hamilton V. E., Bandfield J. L., Glotch T. D., Baldridge A. M., Christensen P. R., Tornabene L. L. and Anderson F. S. (2008) Chloride-bearing materials in the southern highlands of Mars, *Science*, **319**, 1651–1654.

Ozaki K., Tajima S. and Tajika E. (2011) Conditions required for oceanic anoxia/euxinia: Constraints from a one-dimensional ocean biogeochemical cycle model. *Earth and Planetary Science Letters*, **304**, 270–279.

Ozaki K. and Tajika E. (2013) Biogeochemical effects of atmospheric oxygen concentration, phosphorus weathering, and sea-level stand on oceanic redox chemistry: Implications for greenhouse climates. *Earth and Planetary Science Letters*, **373**, 129–139.

Ozaki K., Reinhard, C. T. and Tajika, E. (2018) A sluggish mid-Proterozoic biosphere and its effect on Earth's redox balance. *Geobiology* **17**, 3–11.

Palucis M. C., Dietrich W. E. Williams R. M. E., Hayes A. G., Parker T., Sumner D. W., Mangold N., Lewis K. and Newsom, H. (2016) Sequence and relative timing of large lakes in Gale crater (Mars) after the formation of Mount Sharp, *J. Geophys. Res. Planets*. **121**, 472–496.

Peiffer S. and Gade W. (2007) Reactivity of Ferric Oxides toward H_2S at Low pH. *Environ. Sci. Technol.*, **41**(9), 3159–3164.

Poulet F., Bibring J. P., Mustard J., Gendrin A., Mangold N., Langevin Y., Arvidson R. E., Gondet B., Gomez C. and The Omega Team. (2005) Phyllosilicates on Mars and implications for early martian climate. *Nature,* **438**, 623–627.

Rabinowitch E. (1942) Electron transfer spectra and their photochemical effects. *Reviews of Modern Physics* **14**, 112–131.

Ramirez R. M., Kopparapu R., Zugger M. E., Robinson T. D., Freedman R., and Kasting J. F. (2014) Warming early Mars with CO_2 and H_2. *Nature Geoscience*, **7**, 59–63.

Ramirez R. M. (2017) A warmer and wetter solution for early Mars and the challenges with transient warming. *Icarus*, **297**, 71–82.

Rampe E. B., Bristow T. F., Morris R. V., Morrison S. M., Achilles C. N., Ming D. W., Vaniman D. T., Blake D. F, Tu V. M., Chipera S. J., Yen A. S., Peretyazhko T. S., Downs R. T., Hazen R. M., Treiman A. H., Grotzinger J. P., Castle N., Craig P. I., Des Marais D. J., Thorpe M. T., Walroth R. C., Downs G. W., Fraeman A. A., Siebach K. L., Gellert R., Lafuente B., McAdam A. C., Meslin P.-Y., Sutter B., and Salvatore M. R. (2020) Mineralogy of Vera Rubin ridge from the Mars Science Laboratory CheMin instrument. *Journal of Geophysical Research: Planets*, **125**, e2019JE006306.

Ranjan S. and Sasselov D. D. (2016) Influence of the UV environment on the synthesis of prebiotic molecules. *Astrobiology* **16(1)**, 68-88.

Robbins S. J., Di Achille G. and Hynek B. M. (2011) The volcanic history of Mars: High-resolution crater-based studies of the calderas of 20 volcanoes. *Icarus,* **211**, 1179–1203.

Salese F., Pondrelli M., Neeseman A., Schmidt G. and Ori G. G. (2019). Geological evidence of planet-wide groundwater system on Mars. *Journal of Geophysical Research: Planets*, **124**, 374– 395.

Sander M. U., Luther K. and Troe, J. (1993) On the Photoionization Mechanism of Liquid Water. *Berichte der Bunsengesellschaft für physikalische Chemie,* **97**, 953–960.

Saywell L. G. and Cunningham B. B. (1937) Determination of Iron: Colorimetric o-Phenanthroline Method. *Ind. Eng. Chem. Anal. Ed.* **9**, 67–69.

Seelos F. P., Cartwright F. A., Romeo G. and Murhcie S. L. (2019) Crism Next Generation Mars Global Multispectral Map – Hydrated Mineralogy Spectral Parameter Mappin. *Lunar and Planetary Science Conference L*, abstract #2132.

Stanev E. V., He Y., Staneva J. and Yakushev E. (2014) Mixing in the Black Sea detected from the temporal and spatial variability of oxygen and sulfide – Argo float observations and numerical modelling. *Biogeosciences*, **11**, 5707–5732.

Stefansson A. (2007) Iron(III) hydrolysis and solubility at 25 °C. *Environ.Sci.Technol*. **41**, 6117–123.

Stumm W. and Lee G. F. (1961) Oxygenation of ferrous iron. *Industrial and Engineering Chemistry* **53**, 143–146.

Sung, W. and Morgan, J. J. (1980) Kinetics and product of ferrous iron oxygenation in aqueous systems. *Environmental Science and Technology*, **14**, 561–568.

Tabata H. (2017) Photo-oxidation of ferrous iron as a possible mechanism for acidification on early Mars. Master Thesis, The University of Tokyo.

Tabata H., Sekine Y., Kanzaki Y. and Sugita S. (2021) An experimental study of photo-oxidation of Fe(II): Implications for the formation of Fe(III) (hydro)oxides on early Mars and Earth, *Geochimica et Cosmochimica Acta,* **299**, 35–51.

Tamura, H., Goto, K. and Nagayama, M. (1976) The effect of ferric hydroxide on the oxygenation of ferrous ions in neutral solutions. *Corros. Sci*., **16**,197–207.

Taylor J. R. (1997) An introduction to error analysis, 2nd ed., University Science Boooks, CA, USA.

Thomson B. J., Bridges N. T., Milliken R., Baldridge A., Hook S. J., Crowley J. K., Marion G. M., de Souza Filho C. R., Brown A. J. and Weitz C. M. (2011) Constraints on the origin and evolution of the layered mound in Gale Crater, Mars using Mars Reconnaissance Orbiter data. *Icarus*, **214**, 413-432.

Toon O. B., Segura, T., and Zahnle, K. (2010) The Formation of Martian River Valleys by Impacts. *Annual Review of Earth and Planetary Sciences*, **38**:1, 303–322.

Tosca N. J., McLennan S. M., Clark B. C., Grotzinger J. P., Hurowitz J. A., Knoll A. H., Schröder C. and Squyres S. W. (2005) Geochemical modeling of evaporation

processes on Mars: Insight from the sedimentary record at Meridiani Planum, *Earth and Planet. Sci. Let.* **240**, 122–148.

Tosca N. J., Ahmed I. A. M., Tutolo B. M., Ashpitel A. and Hurowitz J. A. (2018) Magnetite authigenesis and the warming of early Mars. *Nature Geoscience*, **11**, 635–639.

Towe K. M. and Bradley W. F. (1967) Mineralogical constitution of colloidal "hydrous ferric oxides", *Journal of Colloid and Interface Science*, **24** (3), 384–392.

Vaniman D. T., Bish D. L., Ming D. W., Bristow T. F., Morris R. V., Blake D. F., Chipera S. J., Morrison S. M., Treiman A. H., Rampe E. B., Rice M., Achilles C. N., Grotzinger J. P., McLennan S. M., Williams J., Bell III J. F., Newsom H. E., Downs R. T., Maurice S., Sarrazin P., Yen A. S., Morookian A. M., Farmer J. D., Stack K., Milliken R. E., Ehlmann B. L., Sumner D. Y., Berger G., Crisp J. A., Hurowitz J. A., Anderson R., Des Marais D. J., Stolper E. M., Edgett K. S., Gupta S., Spanovich N. and MSL Science Team. (2014) Mineralogy of a Mudstone at Yellowknife Bay, Gale Crater, Mars, *Science,* **343**, 6169.

Viviano-Beck C. E., Seelos F. P., Murchie S. L, Kahn E. G., Seelos K. D., Taylor H. W., Taylor K, Ehlmann B. L., Wiseman S. M., Mustard J. F. and Frank M. (2014) Revised CRISM spectral parameters and summary products based on the currently detected mineral diversity on Mars, *J. Geophys. Res. Planets*, **119**, 1403–1431.

Weitz C. M., Milliken R. E., Grant J. A., McEwen A. S., Williams R. M. E., Bishop J. L., and Thompson B. J. (2010) Mars Reconnaissance Orbiter observations of light-toned layered deposits and associated fluvial landforms on the plateaus adjacent to Valles Marineris, *Icarus,* **205**, 73–102.

Werner S. C. (2009) The global martian volcanic evolutionary history. *Icarus*, **201**, 44–68.

Williams R. M. E., Grotzinger J. P., Dietrich W. E., Gupta S., Sumner D. Y., Wiens R. C., Mangold N., Malin M. C., Edgett K. S., Maurice S., Forni O., Gasnault O., Ollila A., Newsom H. E., Dromart G., Palucis M. C., Yingst R. A., Anderson R. B., Herkenhoff K. E., Le Mouélic S., Goetz W., Madsen M. B., Koefoed A., Jensen J. K., Bridges J. C., Schwenzer S. P., Lewis K. W., Stack K. M., Rubin D., Kah L. C., Bell III J. F., Farmer J. D., Sullivan R., Van Beek T., Blaney D. L., Pariser O., Deen R. G. and MSL Science Team (2013) Martian Fluvial Conglomerates at Gale Crater. *Science,* **340**, 1068–1072.

Wordsworth R. D., Forget, F., Millour, E., Head, J. W., Madeleine, J.-P., and Charnay. B. (2013) Global modelling of the early Martian climate under a denser CO_2 atmosphere: Water cycle and ice evolution. *Icarus*, **222**: 1–19.

Wordsworth R. D., L. Kerber,R. T. Pierrehumbert, F. Forget, and J. W. Head (2015), Comparison of"warm and wet" and "cold and icy"scenarios for early Mars in a 3-Dclimate model. *J. Geophys.Res. Planets*,**120**, 1201–1219.

Wordsworth R., Knoll, A. H., Hurowitz J., Baum M., Ehlmann B. L., Head J. W. and Steakley K. (2021) A coupled model of episodic warming, oxidation and geochemical transitions on early Mars. *Nat. Geosci.* **14**, 127–132.

Wray J. J., Milliken R. E., Dundas C. M., Swayze G. A., Andrews-Hanna J. C., Baldridge A. M., Chojnacki M., Bishop J. L., Ehlmann B. L., Murchie S. L., Clark R. N., Seelos F. P., Tornabene L. L. and Squyres S. W. (2011) Columbus crater and other possible groundwater-fed paleolakes of Terra Sirenum, Mars. *Journal of Geophysical Research,* **116**, E01001.

Zhang X. L., Wu, G. J., Zhang, C. L., Xu, T. L., and Zhou, Q. Q. (2015) What is the real role of iron oxides in the optical properties of dust aerosols? *Atmos. Chem. Phys.*, **15**, 12159–12177.

Ziemniak S. E., Jones M. E. and Combs K. E. S. (1995) Magnetite solubility and phase stability in alkaline media at elevated temperatures. *J. Solution Chem.*, **24**, 837–877.

Zolotov M. Y. and Mironenko M. V. (2016) Chemical models for martian weathering profiles: Insights into formation of layered phyllosilicate and sulfate deposits. *Icarus* **275**, 203–220.